An Estimate of the Coupling of the Sunda Subduction Zone from Campaign and Continuous GPS Data (1991 - 2016)

Chien Zheng YONG[1], Paul H. Denys[1], and Chris F. Pearson[2]

[1]University of Otago
[2]Otago Univ.

November 24, 2022

Abstract

The pre-2004 9.0 Aceh earthquake Global Positioning System (GPS) velocity field along the western margin of the Sunda plate was dominated by the long-term secular velocity and elastic strain. Since then a sequence of the great earthquakes includes the 2005 8.6 Nias, 2007 8.5 Bengkulu, and 2012 8.6 and 8.2 Wharton Basin earthquakes, have occurred in different segments of the subduction zone and its vicinity, which resulted in significant coseismic and postseismic deformation on the Sunda plate. This study combined the published and the estimated GPS velocity fields between 1991–2016 from more than 150 GPS sites. These velocity fields are inverted to examine the angular velocities of the elastic crustal blocks and the variability of the coupling on the subduction trench. This analysis reveals the characteristic of the Sunda subduction interface over multiple earthquake cycles along different segments of the trench, whereby the subduction interface coupling coefficient changed both spatially and temporally after each rupture. The strongly coupled subduction interface along the plate convergence before 2004 earthquake is now partially coupled to freely slipping in the segments that ruptured during the 2005 and 2007 earthquakes, according to the present-day GPS velocity field (2012.2–2016.0). Interestingly, the best fitting model shows that the Siberut segment (0.5–2.0°S) remained fully coupled throughout the years. The result implies that the level of coupling along the highly segmented Sunda subduction interface varies over time, and that the great earthquake rupture was likely to be a result of the variation in the coupling.

An Estimate of the Coupling of the Sunda Subduction Zone from Campaign and Continuous GPS Data (1991 – 2016)

C. Z. Yong[1], P. H. Denys[1], and C. F. Pearson[1]

[1]National School of Surveying, University of Otago, Dunedin, New Zealand

Corresponding author: Chien Zheng Yong (yong.chienzheng@gmail.com)

Key Words:

- Sumatra
- GPS
- active tectonics
- subduction
- tectonic block rotation
- deformation

Key Points:

- We combined 25 years of continuous and campaign-based GPS data to estimate the Sundaland plate velocity field.
- An elastic, rotating block approach is used to explain the plate coupling of the Sundaland subduction interface.
- The Sunda plate coupling shows spatial-temporal variations before and after the 2004 M9.0, 2005 M8.6, 2007 M8.5 and 2012 M8.6 earthquakes.

Abstract

The pre-2004 M_w9.0 Aceh earthquake Global Positioning System (GPS) velocity field along the western margin of the Sunda plate was dominated by the long-term secular velocity and elastic strain. Since then a sequence of the great earthquakes includes the 2005 M_w8.6 Nias, 2007 M_w8.5 Bengkulu, and 2012 M_w8.6 and M_w8.2 Wharton Basin earthquakes, have occurred in different segments of the subduction zone and its vicinity, which resulted in significant coseismic and postseismic deformation on the Sunda plate. This study combined the published and the estimated GPS velocity fields between 1991–2016 from more than 150 GPS sites. These velocity fields are inverted to examine the angular velocities of the elastic crustal blocks and the variability of the coupling on the subduction trench. This analysis reveals the characteristic of the Sunda subduction interface over multiple earthquake cycles along different segments of the trench, whereby the subduction interface coupling coefficient changed both spatially and temporally after each rupture. The strongly coupled subduction interface along the plate convergence before 2004 earthquake is now partially coupled to freely slipping in the segments that ruptured during the 2005 and 2007 earthquakes, according to the present-day GPS velocity field (2012.2–2016.0). Interestingly, the best fitting model shows that the Siberut segment (0.5–2.0°S) remained fully coupled throughout the years. The result implies that the level of coupling along the highly segmented Sunda subduction interface varies over time, and that the great earthquake rupture was likely to be a result of the variation in the coupling.

1 Introduction

Subduction zones constantly store elastic strain energy from the stress build up process due to frictional locking between the tectonic plates. The stored energy will eventually release in a form of either creeping with a longer time interval, and earthquakes with a shorter time interval. Every subduction zone has its unique ability in storing elastic strain, where the degree of locking is subject to a number of factors: (1) the convergence rates and trending (dip angle) of the subduction interface [*Uyeda and Kanamori*, 1979]; (2) temperature of the plate interface [*McCaffrey*, 1993]; (3) age of subducting slab, trench system collision with sediments and seamount ridges [*Kelleher and McCann*, 1976], (4) upper plate deformation [*McCaffrey*, 1993], and (5) other influences (*i.e.* absolute plate motion, back-arc spreading). The role of some of these subduction parameters in subduction locking and seismogenesis may remain controversial [*Pacheco et al.*, 1993; *Hall et al.*, 2003; *Craig and Copley*, 2014], but they certainly play some role in the occurrence of subduction earthquakes. Subduction zones with a high locking coefficient (also known as the degree of coupling) during the interseismic phase, indicates a high level of stress build up, which is likely to lead to a higher likelihood of seismic ruptures [*McCaffrey*, 2002; *Prawirodirdjo et al.*, 2010; *Koulali et al.*, 2017].

The Sunda trench is one of the most tectonically active subduction zones in the world, extending ~5,500 km from the Andaman-Nicobar Islands in the north (°N) to the Sunda Strait in the south (°S). The trench has a rich history of great earthquakes and high potential for generating destructive seismological events (Figure 1). Since after the 2004 M_w 9.0 Aceh giant earthquake, the Sunda subduction zone has undergone an active seismological period. Sequentially, these include the 2005 M_w 8.6 Nias earthquake [*Briggs et al.*, 2006; *Subarya et al.*, 2006; *Banerjee et al.*, 2007; *Konca et al.*, 2007], 2007 M_w 8.5 Bengkulu earthquake [*Konca et al.*, 2008], and the more recent 2012 M_w 8.6 and M_w 8.2 Wharton Basin earthquakes [*Delescluse et al.*, 2012; *Duputel et al.*, 2012; *Meng et al.*, 2012; *Pollitz et al.*, 2012, 2014; *Satriano et al.*, 2012; *Wang et al.*, 2012; *Wiseman and Bürgmann*, 2012; *Yue et al.*, 2012; *Zhang et al.*, 2012; *Wei et al.*, 2013; *Yadav et al.*, 2013; *Geersen et al.*, 2015; *Hill et al.*, 2015; *Yin and Yao*, 2016], have created a significant deformation over the Sunda plate. A long postseismic relaxation period, mainly along the western margin of the Sunda plate, is still influencing the present-day plate motion [*Paul et al.*, 2012; *Yong et al.*, 2017]. *Prawirodirdjo et al.* [2010] showed that the coupling coefficient migrated along the Sunda subduction interface before and after the 2004 and 2005 earthquakes took place. They also showed that the degree of coupling on the subduction interface varied with time, for instance, the locking at the Batu Islands and Enggano segment is spatially varies where it may be triggered by seismic rupture of the subduction fault.

Plate coupling processes on the subduction interface often result in a complex velocity field on the overriding plate [*McCaffrey*, 2002; *Wallace et al.*, 2004]. This complex signal can be observed with geodetic measurements from the cGPS, where the geodetic estimates help to constrain the strain rates and vertical motion rates. Using the geodetic data, this study implements the elastic, rotating block approach [*McCaffrey* 1995, 2002] to model the elastic deformation due to fault coupling over two timescales: (1) long-term tectonic block rotation and (2) short-term (interseismic) elastic deformation due to fault coupling. This modelling approach assumes that the crust of the Earth is comprised of multiple rigid tectonic blocks that are separated by fault lines. These faults can either be coupled (locked) or freely slipping (creeping) during an interseismic period. We model a series of velocity fields over different time periods that are separated by the great earthquakes of: (1) prior to 2004 Aceh earthquake, (2) after the 2005 Nias earthquake and prior to the 2007 Bengkulu earthquake, (3) after the 2007 Bengkulu earthquake and prior to the 2012 Wharton Basin earthquakes, and (4) after the Wharton Basin earthquakes. The first two sets of velocity fields, 1991.0–2001.0 and 2001.0–2007.0, were published and discussed in *Prawirodirdjo et al.* [2010]. This study presents the latter two sets of the new cGPS velocity fields, 2007.0–2012.2 and 2012.2–2015.9, spanning the Sunda forearc and the entire Peninsular Malaysia. This study identifies significant post-seismic deformation present in the geodetic velocity fields, particularly the 2004 M_w 9.0 Aceh and 2012 M_w 8.6 Wharton Basin earthquakes. Thus, this study has obtained a much longer cGPS time series than previously published results [e.g. *Konca et al.*, 2008; *Prawirodirdjo et al.*, 2010]. Based on decades-long cGPS time series, the postseismic deformation were modelled with non-linear decay function (Section 2.1). The corrected velocity fields are introduced to estimate the tectonic coupling of the Sunda subduction interface, as well to verify the spatial distribution of the deformation along the Sunda forearc. For the first time, this study includes the Peninsular Malaysia velocity field in examining the coupling rate (slip rate deficit) on the Sunda subduction zone and other upper plate major fault (*i.e.* the great Sumatran fault).

2 GPS Data Analysis

GPS data from 1999 to 2015 has been used in this study includes the Department of Surveying and Mapping Malaysia's (DSMM) 50 cGPS site network and 48 cGPS sites operated by the Indonesian National Coordinating Agency for Surveys and Mapping (BAKOSURTANAL), Indonesian Institute of Sciences (LIPI), Earth Observatory Singapore (EOS) and California Institute of Technology (Caltech). This study also combined three regional International GPS Service (IGS) sites in Singapore (NTUS), Sumatra (SAMP) and Java Islands (BAKO) into a network of ~100 cGPS sites distributed over the western margin of Sunda plate (Sumatra forearc archipelagos, Sumatra and Peninsular Malaysia). The reference network consists of 41 IGS stations, and these stations are located on stable parts of the tectonic plates as determined in *Altamimi et al.* [2016] (Figure S1).

The cGPS carrier phase data were processed by classical double-differencing technique using the Bernese Software Version 5.2 [*Dach et al.*, 2015] to determine daily relative position estimates. This study applied the Finite Element Solution 2004 (FES2004) ocean loading model from Onsala Space Observatory. We utilised the “CO2 repro2” orbital and clock products from the Centre of Orbit Determination in Europe (CODE) [*Rebischung et al.*, 2016], with the associated antenna phase centre variations files for both satellite and receiver antennas from the IGS. In low-latitude regions, most of the cGPS sites in this study are exposed to a tropical climate famed by large amounts of water vapor in the lower part of the troposphere. These factors increased the challenge of GPS processing data, whereby the tropospheric delays are estimated at two-hour intervals for every site using global mapping function (GMF) for both dry and wet components (Boehm et al., 2006). The estimated site-specific tropospheric parameter in the first attempt is then re-introduced in the second iteration of double-differencing processing, to obtain a high precision solution. An elevation mask angle of 10° was used to avoid the retrieval of the low-latitude total tropospheric zenith path delay. The carrier phase ambiguities are fixed using Bernese’s Quasi-Ionosphere-Free (QIF) strategy and the global ionospheric model by the Centre of Orbit Determination in Europe (CODE). The resulted daily estimates in the International Terrestrial Reference Frame 2008 (ITRF08/IGb08) [*Altamimi et al.*, 2012] were transformed to the Sunda plate-fixed reference frame [*Yong et al.*, 2017] (Section 2.2).

For the processed cGPS measurements, all daily solutions and their covariances were inputted to the Position Time Series (PTS) analysis software [*Denys et al.*, 2014] to isolate the coseismic displacement, postseismic deformation, long-term (secular) site velocity, annual and semi-annual seasonal cycles, and change in velocity rate. The common mode error (CME) of the cGPS sites, such as the orbital and reference frame errors, are simultaneously eliminated by using a spatial correlation filtering technique [*Wdowinski et al.*, 1997]. To establish the commonality between the cGPS sites, *Tian and Shen* [2016] introduced a clustering technique for CME mitigation by splitting a larger network into several sub-networks to improve the correlation for the broadly distributed GPS network. This study adopted their approach by dividing the cGPS network into three smaller clustering networks based on the geographical location of the cGPS sites (Sumatra and Peninsular Malaysia) and data availability to withhold the spatial characteristics at different time spans. The resulting horizontal and vertical components of GPS time series are filtered, and outliers are removed simultaneously before the final velocity estimation. This outlier rejection processes involved the computation of the median and interquartile range (IQR) within 10-day overlapping time windows and omitting solutions that exceed $\pm 3 \times$ IQR criterion [*Beavan*, 2005]. From a total of more than 6,000 station days of data, the outlier rejection removes 0.2–6.0% of the daily solutions for all the position time series with an average of 0.9% rejection rate. The outlier rejection protocol can erroneously mark the seismic signals, on the day of earthquake and its following aftershocks, as outliers. However, as daily positioning solutions cannot determine precise position on the day of the earthquakes, a higher rejection rate is expected close to earthquake events. For example, the near-field sites in Sunda forearc archipelagos typically exhibited a higher level of outliers (4–9%) compare to the remaining far-field sites (<1%). The lower magnitude earthquakes are more likely to affect the position precision of the near-field sites were therefore eliminated by the outlier rejection function.

2.1 Velocity estimation

During the past decade, the Sunda subduction zone and its vicinity has undergone an active seismological period with a sequence of one >M_w 9 giant and four >M_w 8 great earthquakes. In addition to these great events, the cGPS network also detected multiple coseismic displacements from 13 large earthquake events (M_w 7.0–7.9) and more than two dozen moderate earthquakes (M_w 6.0–6.9) that had less seismological impact [*Yong*, 2019]. The impact of the smaller magnitude earthquakes has a smaller spatial extend and less likely to induce any postseismic sequences. In contrast, a great earthquake event will cause a significant coseismic offset in cGPS time series and is often followed by a substantial postseismic transient motion that can persist for decades [*Freymueller et al.*, 2008]. Most of the cGPS sites in this study have detected more than one coseismic and postseismic deformation signals. One of these sites is USMP, amongst the longest spanning cGPS time series, has observed at least four far-field earthquakes. *Yong* [2019] shows that the impact of the postseismic deformation from these great earthquakes are far-reaching, where clear postseismic signals were observed in cGPS site as far as >1,000 km from the epicentre.

The postseismic deformation is often seen as one of the biases that deteriorate the precision of the linear velocities [*Beavan et al.*, 2016]. Decade-long cGPS observation enable a better estimation of the postseismic decay amplitude and decay period that decreases overtime. To mitigate this bias from the time series, the power law, exponential, logarithmic or a combination of the non-linear functions is commonly used to model the postseismic transient. This study suggests that all cGPS time series have achieved a better fit and a lower root-mean-square deviation with logarithmic function for the aforementioned earthquakes than the other non-linear functions. Previous studies [*Savage and Langbein*, 2008; *Feng et al.*, 2015] suggested that using two decay functions could improve the RMS of the time series, as well as the residual fit for the first few days of the major transient events. *Feng et al.* [2015] also propose another approach, which may be suitable to model the postseismic deformation with one decay function and a velocity rate change function. However, this approach shortens the estimated postseismic decay time (from decades to months) compared to using only a single or dual postseismic decay functions approach for a single event [*Feng et al.*, 2015]. Since the cGPS time series may be possible to model with various modelling approaches, extra care must be taken when interpreting cGPS data in complex tectonic regions. This study prefers a single postseismic decay function, as this can retain a reasonable decay period, as well as to simplify in quantifying the spatiotemporal pattern of the amplitude of the postseismic deformation.

All velocity fields in this study are separated by the great earthquakes: (1) the 1991.0–2001.0 with 34 sites; (2) 2001.0–2007.0 with 27 sites; (3) 2007.0–2012.2 with ~90 sites; and (4) 2012.2–2015.9 with ~85 sites (Figure 2). The latter two solutions were estimated from the PTS software [*Denys et al.*, 2014] to determine the cGPS sites velocities and their uncertainties. These velocities are later transformed into the Sunda plate-fixed frame as described in Section 2.2. PTS software involves two processing steps for the velocity estimation. Firstly, the time series was corrected for coseismic, postseismic displacements, and others (*i.e.* seasonal cyclic errors, velocity rate change). Next, the process is follows by the estimation of the long-term velocity using the least squares procedure [*Denys et al.*, 2016].

Another result that came out of the study [*Yong et al.*, 2018] has detected the presence of the groundwater extraction-induced land subsidence, which is mainly affected the cGPS sites along the north-eastern Peninsular Malaysia. The cGPS vertical motion shows a small, but significant, subsidence rate ranging between 1 to 4 mm/yr. The geodetic strain rate analysis estimated a maximum shear strain rate of 0.22 ppm/yr, in which the regional subsidence induced a horizontal component of motion, which in turn biased the horizontal velocity estimation. Nevertheless, the land subsidence is localised and only affected the northern part of Peninsular Malaysia. This study included the five cGPS sites that detected the subside signal in modelling the coupling of the Sunda subduction interface. We found that the localise hydrogeology effect is minimal and did not affecting the outcome of the coupling coefficient by removing these sites.

2.2 Transformation to Sunda-fixed reference frame

To maintain the consistency of the estimated velocity reference frames, we transform the relative velocities from their alignment with the ITRF2008 reference frame to the Sunda plate-fixed frame. Similarly, two published velocity fields from *Prawirodirdjo et al.* [2010] were transformed from ITRF2005 to ITRF2008 and then to the plate-fixed frame. These velocity fields were transformed using a version of the velocity transformation software: Horizontal Time-Dependent Positioning (HTDP) software of *Pearson and Snay* [2013], which was modified to support the transformation into the Sunda-fixed frame. One of the outputs of the software is the Euler pole that transforms the input velocity vectors into the Sunda plate-fixed frame. The Sunda rotation pole is 43.65°N, 86.64°W, and ω = 0.357±0.03°/Ma ($\sigma_{maj/lat^{\circ}}$=4.6, $\sigma_{min/lon^{\circ}}$=2.3, and Azimuth = 116°), which was derived using fifteen cGPS sites from the stable part of the Sunda Block [*Yong et al*., 2017]. These cGPS vectors were determined based on the observation between 1999–2004, the period before 2004 M_w9.0 Aceh and 2005 M_w8.6 Nias earthquakes. Therefore, the postseismic deformation from the recent great earthquakes could be avoided from affecting the linear trend in the cGPS time series. Nevertheless, there is still a concern that the June 2000 earthquakes [*Abercrombie et al*., 2003] could induce postseismic deformation in the south Sumatra region. However, a small coseismic displacement (~4 mm in horizontal and ~8 mm in vertical) was observed at the nearest cGPS site, BAKO, with no sign of a postseismic transient.

3 Data Modelling Approach

To infer the degree of plate coupling along the Sunda subduction interface, this study employed an elastic block inversion approach to interpret the cGPS velocity field [*McCaffrey*, 1995; 2002]. The inversion program, TDEFNODE [*McCaffrey*, 2009a], is used to estimate the surface deformation from the slip deficit in a homogeneous elastic half-space as described by *Okada* [1985]. The back-slip method [*Savage*, 1983] is applied to calculate the elastic contribution around locked fault to the surface velocity field. This study divides the overriding Sunda plate into three distinct blocks: Burma block, Sunda forearc sliver block, and Sunda block, along with the Indian–Australian subducting plate (Figure 3). The boundary configurations of these blocks are distinguished by the Sunda subduction trench, the Sumatran fault system (SFS) [*Sieh and Natawidjaja*, 2000], Andaman Sea back-arc basin [*Curray*, 1989] and other geographical features (*i.e.* volcano belts, mid-ocean ridges).

The boundary of all four elastic crustal blocks are separated by six faults, three out of six are bounding faults that were used to close blocks. These fault lines are used to form the enclosure to block perimeters with nodes only at the surface and they are treated as free-slip boundaries. There other three faults: the Sunda trench, Sumatran Fault System (SFS) and Indian-Burma fault, consist of detailed fault geometries. However, their along-strike nodes are generalised in order to give the best representation of the fault lines at depth. For example, the geomorphic offset along the SFS is ~20 km across the fault [*Sieh and Natawidjaja*, 2000], and there are several published versions of the SFS geometry [*Coffin et al.*, 1998; *Sieh and Natawidjaja*, 2000]. This study used 35 along-strike nodes from *Coffin et al.* [1998] with an average node spacing of 50 km to represent the SFS. Since there are limited GPS observation sites in the eastern of the SFS, we applied a single node parameter index on the SFS as it is more sensible to keep the block model simple and avoid over-parameterisation of the model. Moreover, the cGPS sites between the two sides of the SFS are too far apart (the nearest site in the east of the SFS is ~250 km away) to considered near-field. Lastly, this study compiled a hybrid structural model from *Subarya et al.* [2006; Supplement 6] (0˚–17˚N) and Slab 1.0 model from *Hayes et al.* [2012] (0˚–8.2˚S) to represent the downdip geometry of the Sunda subduction interface. This modified structural model consists of 552 nodes (46 along-strike nodes and 12 down-dip nodes); spaced, on average, every 75 km along-strike, and at depths of 4, 7, 10, 14, 19, 25, 32, 40, 51, 63, 76, and 90 km (Figure 3, inset; see Supplement Information for node positions).

Continuous GPS measurements is used to constrain of the coupling distribution of the subduction interface, as well as the kinematics of the block rotations [*McCaffrey*, 2002; *McCaffrey et al.*, 2007; *Wallace et al.*, 2004]. The degree of coupling along a fault line varies, both spatially and temporally. The coupling can be quantified by estimating the elastic strain that store along the fault line, when two or more adjacent blocks are not freely slipping or locked [*McCaffrey et al.*, 2007]. The fault coupling coefficient (or slip rate fraction) Φ with a range from 0 to 1 is used to describe the region of the fault that is freely slipping ($\Phi = 0$) to strongly coupled ($\Phi = 1$). The slip rate deficit vector $v\Phi$ across the fault is given by multiplying the relative slip rate v by the scalar coupling coefficient Φ. The slip rate deficit reflects the amount of expected interseismic slip on the fault that is not being accommodated by the steady aseismic creep [*McCaffrey*, 2002].

To verify the ability of the cGPS network to resolve the variations in slip rate deficit, a classical checkerboard test is conducted. Firstly, a predefined grid with fully and freely coupled patches along the subduction interface are used to generate a synthetic velocity field. Then, a white noise characteristic of the estimated uncertainties was added to the synthetic velocities (Figure 4a). The synthetic velocities used to estimate the Φ distribution, in which the inversion shows the GPS network successfully detects most part of the subduction trench except for the northern segment of the Sumatra Island (Figure 4b). The cGPS sites in the forearc archipelagos obviously improved the overall resolution of the Φ estimates. However, the checkerboard test indicates that the Φ values are less well resolved for the offshore regions (along strike over a depth of 10 km; ~55 km from the Sunda trench). This is reasonable since the GPS network is restricted to shore, furthermore, there are relatively few cGPS sites in the forearc archipelagos to provide an adequate coverage along the trench.

4 Results from the Best Fitting Model

To evaluate temporal variations in locking between the subducting Indian–Australian plate and the associated overriding blocks, all four velocity fields that each represent a different time period are examined. Hence, each velocity field reflects a different temporal variation of the interseismic coupling. This study performed inversions to estimate the rotation poles for the forearc sliver and the Burma blocks while simultaneously defining the locking coefficient on the subduction interface. The a priori values of these poles are referred to the published values in *Prawirodirdjo et al.* [1997] and *DeMets et al.* [2010]. The estimated rotation pole for the forearc relative to the Sunda plate is near 10.5°N, 87.5°W, and a rotation rate of –0.31°/Ma ± 0.5°/Ma. The rotation pole for the Burma block is 0.9°S, 61.6°W, and ω = 0.68°/Ma, but with very large uncertainties due to the narrow distribution of the observations (Figure 7, inset). Since this study is focused on the temporal change of the coupling coefficient along the subduction trench, the rotation and variable plate coupling are treated as consistent throughout all four periods.

The first set of velocity fields covers the period before the 2004 Aceh and 2005 Nias earthquakes, where it is assumed that the velocity field is stable with minimal long-term interseismic deformation in the region. Between 1991.0 and 2001.0, the best fitting model with reduced χ^2 = 2.41 (68 observations, 40 degrees of freedom (DOF); Table 1 – Model A; Supplementary Information, Figures S3 and S4) inferred full or strong coupling (Φ = 0.8–1.0) from the surface down to a depth of 12 km along the Sunda subduction trench. The southern part of the subduction zone, between the South-Pagai Island and Enggano Island (3.1˚S–5.3˚S), shows a wider and deeper interseismic full-coupled zone down to a depth of 40 km. A similar finding was highlighted by *Prawirodirdjo et al.* [2010], but with a deeper fully locked zone of 50 km. The deeper locking zone is most likely due to a different subduction structural interface, compared to this study, which used a hybrid model from *Subarya et al.* [2006] and *Hayes et al.* [2012]. In contrast, *Prawirodirdjo et al.* [2010] used a similar structural model to *Subarya et al.* [2006] for the northern segment (0˚–17˚N), but the geometry of the southern segment (0˚–8˚S) has not been discussed. Another fully coupled segment is estimated to the north of Nias Island (1.4˚N) extending northwards into the south of Nicobar Island (5.0˚N). However, with limited geodetic measurements covering this region, it may not be possible to conclusively estimate the fault coupling distribution. When Φ is between 0 and 1, it is interpreted as patches with a spatial mixture of creeping and non-creeping states [*McCaffrey et al.*, 2000; *Wallace et al.*, 2004]. This is the case between Nias Island and the Batu Islands (1.4˚N–0.1˚S), whereby the subduction interface in this segment is loosely coupled compared to the neighbouring segments (*i.e.* from the north of Nias Island northwest-ward toward Simeulue Island, and from the south of the Batu Islands southeast-ward toward Enggano Island), particularly below the depth of 14 km. Many studies [*Sieh et al.*, 1999; *Natawidjaja et al.*, 2004; *Feng et al.*, 2015] argue for the presence of aseismic creep, or slow slip events at the Sumatra subduction zone, similar to other subduction zones, *i.e.* the New Zealand–Hikurangi subduction thrust [*Wallace et al.*, 2006] and along the Japan–Bungo Channel [*Hirose et al.*, 1999]. However, the temporal coverage of the cGPS time series analysis in this study may be insufficient to observe the presence of slow slip events, given that *Tsang et al.* [2015] suggest this process can takes approximately 15 years. Hence, the theory that suggests that the low rates of interseismic coupling below and trenchward of the Batu Islands remains debatable.

The interseismic velocity field that covers the period 2001.0–2007.0 was assembled based on a mixture of the campaign-based GPS data and cGPS data in *Prawirodirdjo et al.* [2010]. They excluded the model of the interseismic coupling in the northern region of the Sumatra forearc, which was dominated by the Aceh and Nias earthquakes postseismic deformation. Clear postseismic deformation trends were observed at the near field stations between northern Simeulue and the Batu islands (Figure 1a). However, their study did not explicitly discuss the influence of Aceh and Nias postseismic afterslips that is likely to remain in the estimated velocity vectors. This transient postseismic deformation is also observed by the cGPS measurements that a substantial postseismic afterslip is found on the western margin of the Sunda plate [*Yong et al*., 2017]. For the 2001.0–2007.0 velocity field, the best fit model of the Sumatra forearc obtained a reduced χ^2=3.50 (54 observations, 26 DOF; Table 1 – Model B). Poor spatial coverage of GPS sites in the northern segment, from south of Nias Island (~0.1˚N) to Nicobar Island (~5.0˚N), limits a reliable estimation on the interseismic coupling coefficient that in this case shows a freely slipping interface (Φ = 0, depth >4 km) with low levels of coupling. Additionally, the presence of postseismic deformation from the 2004 Aceh and 2005 Nias earthquakes could dominate the locking signals in the northern segment. Further south, the velocity fields in the Batu Islands are consistent with a low to partially coupled subduction zone (Φ = ≤ 0.5). Aseismic surface creep on the subduction interface is likely to be present around the Batu Islands [*Simoes et al.*, 2004], therefore, no constraint is imposed on the Φ values of the fault node as it decreases downdip from the surface. There is partial interseismic coupling (Φ = 0.5–0.8) on the subduction interface from Siberut Island down to Enggano Island, where the best fit model indicates that the coupling is down to a depth of ~20 km.

Similarly, the 2007.0–2012.2 velocity field estimated from the cGPS data in this study is affected by the postseismic deformation of the Aceh and Nias earthquakes (Figure 2a). The velocity field between 2007.0 and 2012.2 is derived solely from the cGPS data. The northern part of the Sumatra forearc (0.8˚N and above) continues to be dominated by the significant postseismic deformation following the Aceh and Nias earthquakes in the velocity field. The postseismic deformation signal also influences the velocity field in Peninsular Malaysia, especially in the northwest region, which caused a systematic misfit in the model (Figure 5a). The best fit 2007.0–2012.2 model (reduced χ^2= 3.82; 228 observations, 130 DOF; Table 1 – Model C) infers that the subduction interface underneath Simeulue Island has a Φ value close to 1.0. A high coupling coefficient (Φ = 0.5–0.8) is also found in-between Siberut Island and north of Enggano Island (1.3˚S–5.5˚S), with a slight drop of the locking rate below a depth of 14 km, which is related to the 2007 Bengkulu earthquake. Large earthquakes often rupture areas that were previously locked during the interseismic period [*Konca et al.*, 2008; *Kaneko et al.*, 2010]. Our best fit model agrees with *Konca et al.* [2008] suggesting that the Bengkulu earthquake has only partially released the interseismic strain accumulated since 1833 [*Newcomb and McCann*, 1987; *Natawidjaja et al.*, 2006]. The possibility of future great earthquakes in this segment remains conceivably high.

The post-2012 interseismic velocity field, which represents the present-day Sunda plate motion, includes a combination of postseismic afterslip of the Aceh, Nias and Wharton Basin earthquakes (Figure 5b). This result highlights that the postseismic signal from the 2004 and 2005 earthquakes is less prominent after the 2012 Wharton Basin earthquakes. This suggests that the postseismic deformation within the Sunda plate has decayed significantly since the Aceh and Nias earthquakes. The best fitting model obtain reduced χ^2 =1.29 (226 observations, 190 DOF; Table 1 – Model D). This model indicates that the Sunda trench has partially regained the interseismic coupling from Simeulue Island south eastward towards Enggano Island, and from the surface down to a depth of ~7 km. Whereas, the subduction interface underneath Siberut and Pagai Islands is still fully locked at the surface. The coupling gradually decreases to ~40 km depth. The patch underneath Siberut Island remains locked at the surface, but the locking gradually decreases to a level of low coupling at ~40 km depth since after the 2004 Aceh earthquake. On the other hand, the long-term aseismic behaviour underneath the Batu Islands [*Natawidjaja et al.*, 2006] reflects the partial or no coupling, which agrees with earlier geodetic and geophysical studies [*Natawidjaja et al.*, 2004; *Prawirodirdjo et al.*, 2010]. Although still uncertain, the most cited reason for low coupling in this segment is possibly caused by the subduction of the Investigator Fracture Zone (IFZ; Figure 1a) [*Prawirodirdjo et al.*, 1997; *McCaffrey*, 2002; *Chlieh et al.*, 2008; *Lange et al.*, 2010; *Prawirodirdjo et al.*, 2010]. This study agrees on the previous studies [*Briggs et al.*, 2006; *Chlieh et al.*, 2008; *Lange et al.*, 2010], whereby this patch acts as a natural barrier to inhibit further propagation of earthquake rupture along the Sunda and Java trenches.

To summarise the current state for the Sundaland subduction trench, Figure 7 shows the modelled post-2012 horizontal velocity field. The edge of the Sunda forearc converge margin-normal to the trench but shifts to margin parallel near the Sumatran fault system. *McCaffrey* [2002] explained that the indication of partitioning is when the deformation is contractional near the trench and transitions to margin-parallel shear further landward. Hence, in this case, the block model results and the GPS measurements both demonstrate that Sumatra is highly partitioned. The coupling coefficient along the Sunda trench shows episodic variation, which is largely influenced by the occurrence of the great earthquake.

5 Summary

More than 25 years of GPS velocity field estimates has been compiled from published results (1991.0 – 2007.0) and new cGPS data (2007.0 – 2016.0). The velocity field data, distributed across the Sunda forearc archipelagos, Sumatra and Peninsular Malaysia, has been used to study the subduction interface behaviour through a series of four great earthquakes. The data covers different stages of the earthquake cycle, including the end of an interseismic period, entering one or more postseismic deformation periods, and probably beginning of a new interseismic cycle.

The deformation along the Sunda subduction trench is dominated by postseismic deformation that followed after a series of earthquakes, as well as the elastic strain from spatially variable slip rate deficits on the subduction interface. From the northernmost segment, comprising the Andaman–Simeulue segment (> 3°N), the patch that was fully locked before the Aceh earthquake has entered a freely slipping phase after the rupture. The latest velocity fields indicate that this segment is partially coupled on the shallow part of the subduction zone (from the surface of the trench to a depth of 10 km). This segment will eventually regain the potential for another earthquake event. Further south, the locking coefficient in Simeulue–Nias segment (3° – 0.5°N), the patch that ruptured during the 2005 Nias earthquake, has undergone an identical process as the Andaman-Simeulue segment. The present-day velocity field shows a moderate degree of coupling in this segment at the surface down to ~20 km in depth. The Nias–Batu segment (0.5°N – 0.5°S) suggests that the subduction interface is loosely coupled to freely slipping for all four time periods. This patch is believed to act like an inhibitor to restrict the earthquake rupture that could potentially propagates along the Sunda and Java trenches [*Briggs et al.*, 2006; *Prawirodirdjo et al.*, 2010]. Before the Aceh earthquake, the adjacent patch of Batu and north Pagai Islands (0.5° – 2.8°S) shows a strong plate coupling from the surface, and the coupling coefficient is gradually decreased to a depth of 20 km. Subsequently, the coupling coefficient for this segment is stretched to a depth of ~40 km, and this locked subduction interface has persisted through multiple earthquake cycles. The past reports [*Konca et al.*, 2008; *Wiseman and Bürgmann*, 2011] have suggested that the energy was partially released in the 2007 M_w 8.5 and M_w 7.9 Bengkulu earthquakes. Therefore, the risk of earthquake and tsunami threat remains high in this segment. Lastly, the southernmost segment of the Sunda subduction trench, the South-Pagai – Enggano Islands segment (3.1˚S–5.3˚S), is the segment where the 4th June 2000 M_w 7.9 and 2007 M_w 8.5 Bengkulu earthquakes were occurred. The subduction interface of this segment indicates a different interseismic deformation pattern than other segments, where this segment was mainly influenced by the two aforementioned earthquakes. This segment indicates a locked interseismic deformation pattern from the surface to depth ~40 km in the pre-2007 Bengkulu earthquake, and then freely slipping from depth >14 km after the rupture. The current deformation in this segment is parallel with the condition of the post-2007 Bengkulu earthquake, whereby the chance of reoccurrence of the 1833 earthquake remains highly plausible.

Acknowledgments

The authors would like to acknowledge the International GNSS Services (IGS), Center for Orbit Determination in Europe (CODE), Badan Informasi Geospasial (BIG), Indonesian Institute of Science (LIPI), Caltech Tectonics Observatory and Earth Observatory of Singapore (EOS) for maintaining and making the GPS/GNSS data and processing parameter available. We would like to specially thank to Department of Surveying and Mapping Malaysia (DSMM) for providing continuous GPS data from Malaysia under the copyright license No. JUPEM.BPK.18/4/16.10 (151) and JUPEM.BP.07.01.14 (63). We would also like to thank Robert McCaffrey for making TDEFNODE – Elastic dislocation model software available. This work is also benefited from Jeff Freymueller and Laura Wallace for their insights and comments in the PhD defense.

References

Abercrombie, R. E., Antolik, M. and Ekström, G. (2003), The June 2000 *Mw* 7.9 earthquakes south of Sumatra: Deformation in the India–Australia Plate *J. Geophys. Res.*, *Solid Earth*, 108 (B1), 2018. doi: 10.1029/2001JB000674

Altamimi, Z., L. Métivier, and X. Collilieux (2012), ITRF2008 plate motion model, *J. Geophys. Res., Solid Earth*, 117(B7), B07402, doi: 10.1029/2011JB008930.

Altamimi, Z., Rebischung, P., Métivier, L. and Collilieux, X. (2016), ITRF2014: A new release of the International Terrestrial Reference Frame modeling nonlinear station motions. *J. Geophys. Res., Solid Earth*, 121, 6109-6131. doi: 10.1002/2016JB013098.

Banerjee, P., F. Pollitz, B. Nagarajan, and R. Bürgmann (2007), Coseismic Slip Distributions of the 26 December 2004 Sumatra–Andaman and 28 March 2005 Nias Earthquakes from GPS Static Offsets, *Bull. Seismol. Soc. Am.*, 97(1A), S86–S102, doi: 10.1785/0120050609.

Beavan, J. (2005), Noise properties of continuous GPS data from concrete pillar geodetic monuments in New Zealand and comparison with data from U.S. deep drilled braced monuments. *J. Geophys. Res., Solid Earth*, 110(B8), B08410. doi:10.1029/2005JB003642.

Beavan, J., L. M. Wallace, N. Palmer, P. Denys, S. Ellis, N. Fournier, S. Hreinsdottir, C. Pearson, and M. Denham (2016), New Zealand GPS velocity field: 1995–2013, *New Zeal. J. Geol. Geophys.*, 59(1), 5-14, doi:10.1080/00288306.2015.1112817.

Bird, P. (2003), An updated digital model of plate boundaries. *Geochem. Geophy. Geosy.*, 4, 1027. doi: 10.1029/2001GC000252

Briggs, R. W., K. Sieh, A. J. Meltzner, D. Natawidjaja, J. Galetzka, B. Suwargadi, Y.-j. Hsu, M. Simons, N. Hananto, I. Suprihanto, D. Prayudi, J.-P. Avouac, L. Prawirodirdjo and Y. Bock (2006), Deformation and Slip Along the Sunda Megathrust in the Great 2005 Nias-Simeulue Earthquake, *Science*, 311(5769), 1897–1901, doi: 10.1126/science.1122602.

Boehm, J., Werl, B., and Schuh, H. (2006), Troposphere Mapping Functions for GPS and Very Long Baseline Interferometry from European Centre for Medium-Range Weather Forecasts Operational Analysis Data. *J. Geophys. Res., Solid Earth*, 111, B02406, doi:10.1029/2005JB003629.

Chlieh, M., J. P. Avouac, K. Sieh, D. H. Natawidjaja, and J. Galetzka (2008), Heterogeneous coupling of the Sumatran megathrust constrained by geodetic and paleogeodetic measurements, *J. Geophys. Res., Solid Earth*, 113(B5), B05305, doi: 10.1029/2007JB004981.

Coffin, M.F., Gahagan, L.M., and Lawver, L.A., (1998), *Present-day Plate Boundary Digital Data Compilation*. University of Texas Institute for Geophysics Technical Report No. 174, pp. 5.

Craig, T. J., and A. Copley (2014), An explanation for the age independence of oceanic elastic thickness estimates from flexural profiles at subduction zones, and implications for continental rheology, *Earth Planet. Sci. Lett.*, *392*, 207-216, doi: 10.1016/j.epsl.2014.02.027.

Curray, J. R. (1989), The Sunda Arc: A model for oblique plate convergence, *Neth. J. Sea Res.*, 24(2), 131–140, doi: 10.1016/0077-7579(89)90144-0.

Dach, R., S. Lutz, P. Walser, and P. Fridez (2015), *Bernese GNSS Software Version 5.2*. User manual, Bern Open Publishing, Astronomical Institute, University of Bern.

Delescluse, M., N. Chamot-Rooke, R. Cattin, L. Fleitout, O. Trubienko, and C. Vigny (2012), April 2012 intra-oceanic seismicity off Sumatra boosted by the Banda-Aceh megathrust, *Nature*, 490(7419), 240–244, doi: 10.1038/nature11520.

Denys, P., Norris, R., Pearson, C., and Denham, M. (2014), A Geodetic Study of the Otago Fault System of the South Island of New Zealand. In C. Rizos & P. Willis (Eds.), *Earth on the Edge: Science for a Sustainable Planet*: Proceedings of the IAG General Assembly, Melbourne, Australia, June 28–July 2, 2011 (pp. 151-158). Berlin, Heidelberg: Springer Berlin Heidelberg.

Denys, P., and C. Pearson (2016), *Positioning in Active Deformation Zones - Implications for NetworkRTK and GNSS Processing Engines*, Proceedings of the FIG Working Week 2016, Christchurch, New Zealand, May 2-6.

Duputel, Z., H. Kanamori, V. C. Tsai, L. Rivera, L. Meng, J.-P. Ampuero, and J. M. Stock (2012), The 2012 Sumatra great earthquake sequence, *Earth Planet. Sci. Lett.*, 351–352, 247–257, doi: 10.1016/j.epsl.2012.07.017.

Ekström, G., M. Nettles, and A. M. Dziewonski (2012), The global CMT project 2004-2010: Centroidmoment tensors for 13,017 earthquakes, *Phys. Earth Planet. Int.*, 200-201, 1-9. doi: 10.1016/j.pepi.2012.04.002

Feng, L., Hill, E. M., Banerjee, P., Hermawan, I., Tsang, L. L. H., Natawidjaja, D. H., Suwargadi, B. W. and Sieh, K. (2015), A unified GPS-based earthquake catalog for the Sumatran plate boundary between 2002 and 2013. *J. Geophys. Res., Solid Earth*, 3566-3598. doi: 10.1002/2014JB011661

Freymueller, J. T., Woodard, H., Cohen, S. C., Cross, R., Elliott, J., Larsen, C. F., Hreinsdóttir, S. and Zweck, C. (2008), Active Deformation Processes in Alaska, Based on 15 Years of GPS Measurements. In: Freymueller, J. T., Haeussler, P. J., Wesson, R. L. and Ekström, G. (eds.) *Active Tectonics and Seismic Potential of Alaska*. Washington, D. C.: American Geophysical Union, pp. 1–42. doi: 10.1029/179GM02

Geersen, J., J. M. Bull, L. C. McNeill, T. J. Henstock, C. Gaedicke, N. Chamot-Rooke, and M. Delescluse (2015), Pervasive deformation of an oceanic plate and relationship to large $>M_w$ 8 intraplate earthquakes: The northern Wharton Basin, Indian Ocean, *Geology*, 43(4), 359–362, doi: 10.1130/g36446.1.

Hall, C. E., M. Gurnis, M. Sdrolias, L. L. Lavier, and R. D. Müller (2003), Catastrophic initiation of subduction following forced convergence across fracture zones, *Earth Planet. Sci. Lett.*, *212*(1), 15-30, doi: 10.1016/S0012-821X(03)00242-5.

Hayes, G. P., Wald, D. J. and Johnson, R. L. (2012), Slab1.0: A three-dimensional model of global subduction zone geometries. *J. Geophys. Res., Solid Earth*, 117, B01302. doi: 10.1029/2011JB008524

Hill, E. M., Yue, H., Barbot, S., Lay, T., Tapponnier, P., Hermawan, I., Hubbard, J., Banerjee, P., Feng, L., Natawidjaja, D. and Sieh, K. (2015), The 2012 M_w 8.6 Wharton Basin sequence: A cascade of great earthquakes generated by near-orthogonal, young, oceanic mantle faults. *J. Geophys. Res., Solid Earth*, 120, 3723-3747. doi: 10.1002/2014JB011703.

Hirose, H., K. Hirahara, F. Kimata, N. Fujii, and S. i. Miyazaki (1999), A slow thrust slip event following the two 1996 Hyuganada Earthquakes beneath the Bungo Channel, southwest Japan, *Geophys. Res. Lett.*, 26(21), 3237-3240, doi:10.1029/1999GL010999.

Hurukawa, N., B. R. Wulandari, and M. Kasahara (2014), Earthquake History of the Sumatran Fault, Indonesia, since 1892, Derived from Relocation of Large Earthquakes, *Bull. Seismol. Soc. Am.*, 104(4), 1750-1762, doi: 10.1785/0120130201.

JMG (2009), Minerals and Geoscience Department Malaysia – *Seismotectonic Map of Malaysia 5th edition*. (Printed map)

Kaneko, Y., J.-P. Avouac, and N. Lapusta (2010), Towards inferring earthquake patterns from geodetic observations of interseismic coupling, *Nat. Geosci.*, 3, 363, doi: 10.1038/ngeo843.

Kelleher, J., and W. McCann (1976), Buoyant zones, great earthquakes, and unstable boundaries of subduction, *J. Geophys. Res.*, 81(26), 4885–4896, doi: 10.1029/JB081i026p04885.

Konca, A. O., V. Hjorleifsdottir, T.-R. A. Song, J.-P. Avouac, D. V. Helmberger, C. Ji, K. Sieh, R. Briggs, and A. Meltzner (2007), Rupture Kinematics of the 2005 M_w 8.6 Nias–Simeulue Earthquake from the Joint Inversion of Seismic and Geodetic Data, *Bull. Seismol. Soc. Am.*, 97(1A), S307–S322, doi: 10.1785/0120050632.

Konca, A. O., Avouac, J.-P., Sladen, A., Meltzner, A. J., Sieh, K., Fang, P., Li, Z., Galetzka, J., Genrich, J., Chlieh, M., Natawidjaja, D. H., Bock, Y., Fielding, E. J., Ji, C. and Helmberger, D. V. (2008), Partial rupture of a locked patch of the Sumatra megathrust during the 2007 earthquake sequence. *Nature*, 456, 631-635. doi: 10.1038/nature07572.

Koulali, A., S. McClusky, S. Susilo, Y. Leonard, P. Cummins, P. Tregoning, I. Meilano, J. Efendi, and A. B. Wijanarto (2017), The kinematics of crustal deformation in Java from GPS observations: Implications for fault slip partitioning, *Earth Planet. Sci. Lett.*, *458*, 69–79, doi: 10.1016/j.epsl.2016.10.039.

Lange, D., F. Tilmann, A. Rietbrock, R. Collings, D. H. Natawidjaja, B. W. Suwargadi, P. Barton, T. Henstock, and T. Ryberg (2010), The Fine Structure of the Subducted Investigator Fracture Zone in Western Sumatra as Seen by Local Seismicity, *Earth Planet. Sci. Lett.*, *298*(1), 47-56, doi:10.1016/j.epsl.2010.07.020.

McCaffrey, R. (1993), On the role of the upper plate in great subduction zone earthquakes, *J. Geophys. Res., Solid Earth*, 98(B7), 11953–11966, doi: 10.1029/93JB00445.

McCaffrey, R., P. C. Zwick, Y. Bock, L. Prawirodirdjo, J. F. Genrich, C. W. Stevens, S. S. O. Puntodewo, and C. Subarya (2000), Strain partitioning during oblique plate convergence in northern Sumatra: Geodetic and seismologic constraints and numerical modeling, *J. Geophys. Res., Solid Earth*, 105(B12), 28363-28376, doi: 10.1029/1999JB900362.

McCaffrey, R. (2002), Crustal Block Rotations and Plate Coupling, in Plate Boundary Zones, *American Geophys. Union*, pp. 101–122, Washington DC.

McCaffrey, R., Qamar, A. I., King, R. W., Wells, R., Khazaradze, G., Williams, C. A., Stevens, C. W., Vollick, J. J. and Zwick, P. C. (2007), Fault locking, block rotation and crustal deformation in the Pacific Northwest. *Geophys. J. Int.*, 169, 1315–1340, doi: 10.1111/j.1365-246X.2007.03371.x.

McCaffrey, R. (2009a), Time-dependent inversion of three-component continuous GPS for steady and transient sources in northern Cascadia. *Geophys. Res. Lett.*, 36, L07304. doi: 10.1029/2008GL036784

McCaffrey, R. (2009b), The Tectonic Framework of the Sumatran Subduction Zone. *Annu. Rev. Earth Planet. Sci.*, 37, 345-366. doi: 10.1146/annurev.earth.031208.100212.

Meng, L., J.-P. Ampuero, J. Stock, Z. Duputel, Y. Luo, and V. C. Tsai (2012), Earthquake in a Maze: Compressional Rupture Branching During the 2012 M_w 8.6 Sumatra Earthquake, *Science*, 337(6095), 724–726, doi: 10.1126/science.1224030.

Natawidjaja, D. H., K. Sieh, S. N. Ward, H. Cheng, R. L. Edwards, J. Galetzka, and B. W. Suwargadi (2004), Paleogeodetic records of seismic and aseismic subduction from central Sumatran microatolls, Indonesia, *J. Geophys. Res., Solid Earth*, 109(B4), B04306, doi: 10.1029/2003JB002398.

Natawidjaja, D. H., Sieh, K., Chlieh, M., Galetzka, J., Suwargadi, B. W., Cheng, H., Edwards, R. L., Avouac, J.-P. and Ward, S. N. (2006), Source parameters of the great Sumatran megathrust earthquakes of 1797 and 1833 inferred from coral microatolls. *J. Geophys. Res., Solid Earth*, 111, B06403. doi: 10.1029/2005JB004025

Newcomb, K. R. and McCann, W. R. (1987), Seismic history and seismotectonics of the Sunda Arc. *J. Geophys. Res., Solid Earth*, 92, 421-439. doi: 10.1029/JB092iB01p00421

Okada, Y. (1985), Surface deformation due to shear and tensile faults in a half-space. *Bull. Seismol. Soc. Am.*, 75, 1135-1154.

Pacheco, J. F., L. R. Sykes, and C. H. Scholz (1993), Nature of seismic coupling along simple plate boundaries of the subduction type, *J. Geophys. Res., Solid Earth*, 98(B8), 14133–14159, doi: 10.1029/93JB00349.

Paul, J., C. P. Rajendran, A. R. Lowry, V. Andrade, and K. Rajendran (2012), Andaman Postseismic Deformation Observations: Still Slipping after All These Years?, *Bull. Seismol. Soc. Am.*, 102(1), 343–351, doi: 10.1785/0120110074.

Pearson, C. F., and R. Snay (2013), Introducing HTDP 3.1 to transform coordinates across time and spatial reference frames, *GPS Solut.*, 17(1), 1-15, doi: 10.1007/s10291-012-0255-y.

Pollitz, F. F., R. S. Stein, V. Sevilgen, and R. Burgmann (2012), The 11 April 2012 east Indian Ocean earthquake triggered large aftershocks worldwide, *Nature*, 490(7419), 250–253, doi: 10.1038/nature11504.

Pollitz, F. F., R. Bürgmann, R. S. Stein, and V. Sevilgen (2014), The Profound Reach of the 11 April 2012 M 8.6 Indian Ocean Earthquake: Short-Term Global Triggering Followed by a Longer-Term Global Shadow, *Bull. Seismol. Soc. Am.*, 104(2), 972–984, doi: 10.1785/0120130078.

Prawirodirdjo, L., Bock, Y., McCaffrey, R., Genrich, J., Cakausm E., Stevens, C., Puntodewo, S. S. O., Subarya, C., Rais, J., Zwick, P., and Fauzi. (1997), Geodetic observations of interseismic strain segmentation at the Sumatra Subduction Zone, *Geophys. Res. Lett.*, 24(21), 2601-2604, doi: 10.1029/97GL52691.

Prawirodirdjo, L., R. McCaffrey, C. D. Chadwell, Y. Bock, and C. Subarya (2010), Geodetic observations of an earthquake cycle at the Sumatra subduction zone: Role of interseismic strain segmentation, *J. Geophys. Res.*, *Solid Earth*, *115*(B3), B03414, doi:10.1029/2008JB006139.

Rebischung, P., Z. Altamimi, J. Ray, and B. Garayt (2016), The IGS contribution to ITRF2014, *J. Geod.*, 90(7), 611-630, doi: 10.1007/s00190-016-0897-6.

Satriano, C., E. Kiraly, P. Bernard, and J.-P. Vilotte (2012), The 2012 M_w 8.6 Sumatra earthquake: Evidence of westward sequential seismic ruptures associated to the reactivation of a N-S ocean fabric, *Geophys. Res. Lett.*, 39(15), L15302, doi: 10.1029/2012GL052387.

Savage, J. C. (1983), Strain Accumulation in Western United States. *Annu. Rev. Earth Planet. Sci.*, 11, 11-41. doi: 10.1146/annurev.ea.11.050183.000303

Savage, J. C. and J. Langbein (2008), Postearthquake relaxation after the 2004 M6 Parkfield, California, earthquake and rate-and-state friction. *J. Geophys. Res., Solid Earth*, 113, B10407. doi: 10.1029/2008JB005723

Sieh, K., S. N. Ward, D. Natawidjaja, and B. W. Suwargadi (1999), Crustal deformation at the Sumatran Subduction Zone revealed by coral rings, *Geophys. Res. Lett.*, 26(20), 3141-3144, doi:10.1029/1999GL005409.

Sieh, K. and D. Natawidjaja, (2000), Neotectonics of the Sumatran fault, Indonesia. *J. Geophys. Res.*, *Solid Earth*, 105, 28295–28326, doi: 10.1029/2000JB900120.

Simandjuntak, T. O. and Barber, A. J. (1996), *Contrasting tectonic styles in the Neogene orogenic belts of Indonesia*. Geological Society (London) Special Publication, 106, 185–201. doi: 10.1144/gsl.sp.1996.106.01.12.

Simoes, M., J. P. Avouac, R. Cattin, and P. Henry (2004), The Sumatra subduction zone: A case for a locked fault zone extending into the mantle, *J. Geophys. Res., Solid Earth*, 109(B10), B10402, doi: 10.1029/2003JB002958.

Singh, S. C. and Moeremans, R. (2017), Chapter 13: Anatomy of the Andaman–Nicobar subduction system from seismic reflection data. In: Bandopadhyay, P. C. and Carter, A. (eds) *The Andaman–Nicobar Accretionary Ridge: Geology, Tectonics and Hazards*. Geological Society, London, Memoirs, 47, 225–232, doi: 10.1144/M47.16.

Subarya, C., M. Chlieh, L. Prawirodirdjo, J.-P. Avouac, Y. Bock, K. Sieh, A. J. Meltzner, D. H. Natawidjaja, and R. McCaffrey (2006), Plate-boundary deformation associated with the great Sumatra–Andaman earthquake, *Nature*, 440(7080), 46–51, doi: 10.1038/nature04522.

Tian, Y., and Shen, Z.-K. (2016), Extracting the regional common-mode component of GPS station position time series from dense continuous network. *J. Geophys. Res., Solid Earth*, 121(2), 1080-1096. doi:10.1002/2015JB012253

Tsang, L. L. H., A. J. Meltzner, B. Philibosian, E. M. Hill, J. T. Freymueller, and K. Sieh (2015), A 15 year slow-slip event on the Sunda megathrust offshore Sumatra, *Geophys. Res. Lett.*, 6630-6638, doi: 10.1002/2015GL064928.

Uyeda, S., and H. Kanamori (1979), Back-arc opening and the mode of subduction, *J. Geophys. Res.*, *Solid Earth*, 84(B3), 1049–1061, doi: 10.1029/JB084iB03p01049.

Wallace, L. M., J. Beavan, R. McCaffrey, and D. Darby (2004), Subduction zone coupling and tectonic block rotations in the North Island, New Zealand, *J. Geophys. Res., Solid Earth*, 109(B12), B12406, doi: 10.1029/2004JB003241.

Wallace, L. M., and J. Beavan (2006), A large slow slip event on the central Hikurangi subduction interface beneath the Manawatu region, North Island, New Zealand, *Geophys. Res. Lett.*, 33(11), L11301, doi: 10.1029/2006GL026009.

Wang, D., J. Mori, and T. Uchide (2012), Supershear rupture on multiple faults for the M_w 8.6 Off Northern Sumatra, Indonesia earthquake of April 11, 2012, *Geophys. Res. Lett.*, 39(21), L21307, doi: 10.1029/2012GL053622.

Wdowinski, S., Bock, Y., Zhang, J., Fang, P., and Genrich, J. (1997), Southern California permanent GPS geodetic array: Spatial filtering of daily positions for estimating coseismic and postseismic displacements induced by the 1992 Landers earthquake. *J. Geophys. Res., Solid Earth*, 102(B8), 18057-18070. doi:10.1029/97JB01378

Wiseman, K., and R. Bürgmann (2011), Stress and Seismicity Changes on the Sunda Megathrust Preceding the 2007 M_w 8.4 Earthquake, *Bull. Seismol. Soc. Am.*, *101*(1), 313-326, doi:10.1785/0120100063.

Wiseman, K., and R. Bürgmann (2012), Stress triggering of the great Indian Ocean strike-slip earthquakes in a diffuse plate boundary zone, *Geophys. Res. Lett.*, 39(22), L22304–L22309, doi: 10.1029/2012GL053954.

Wei, S., D. Helmberger, and J.-P. Avouac (2013), Modeling the 2012 Wharton basin earthquakes off-Sumatra: Complete lithospheric failure, *J. Geophys. Res., Solid Earth*, 118(7), 3592–3609, doi: 10.1002/jgrb.50267.

Yadav, R. K., B. Kundu, K. Gahalaut, J. Catherine, V. K. Gahalaut, A. Ambikapthy, and M. S. Naidu (2013), Coseismic offsets due to the 11 April 2012 Indian Ocean earthquakes (M_w 8.6 and 8.2) derived from GPS measurements, *Geophys. Res. Lett.*, 40(13), 3389–3393, doi: 10.1002/grl.50601.

Yin, J., and H. Yao (2016), Rupture and Frequency-dependent Seismic Radiation of the 2012 M_w 8.6 Sumatra Strike-slip Earthquake, *Geophys. J. Int.*, 205(3), 1682–1693, doi: 10.1093/gji/ggw105.

Yong, C. Z., P. H. Denys, and C. F. Pearson (2017), Present-day kinematics of the Sundaland plate, *J. Appl. Geodesy*, 11(3), 169, doi: 10.1515/jag-2016-0024.

Yong, C. Z., Denys, P. and Pearson, C. (2018), Groundwater extraction-induced land subsidence: a geodetic strain rate study in Kelantan, Malaysia, *J. Spat. Sci.*. doi: 10.1080/14498596.2018.1429329

Yong, C. Z. (2019), An Analysis of the Crustal Deformation of the Western Sundaland Plate from Nearly Two Decades of continuous GPS Measurements, *Ph.D thesis*, Univ. of Otago, Dunedin, New Zealand. Available on: https://ourarchive.otago.ac.nz/handle/10523/9484

Yue, H., T. Lay, and K. D. Koper (2012), En echelon and orthogonal fault ruptures of the 11 April 2012 great intraplate earthquakes, *Nature*, 490(7419), 245–249, doi: 10.1038/nature11492.

Zhang, H., J. Chen, and Z. Ge (2012), Multi-fault rupture and successive triggering during the 2012 M_w 8.6 Sumatra offshore earthquake, *Geophys. Res. Lett.*, 39(22), L22305, doi: 10.1029/2012GL053805.

Table 1. The inversion results for locking and rotation models

Model	T	N_{GPS}	f_{GPS}	$\chi_{GPS}{}^2$	χ^2	N_{data}	N_p	DOF	$\chi_v{}^2$
A	1991.0–2001.0	34	2.0	1.179	80.17	68	28	40	2.408
B	2001.0–2007.0	27	4.0	1.293	69.82	54	28	26	3.495
C	2007.0–2012.2	122	4.0	1.470	335.16	228	98	130	3.821
D	2012.2–2015.9	123	4.0	1.033	233.46	226	36	190	1.296

Note: T = period of measurement. N_{GPS} = number of GPS observations (N, E and U velocities are treated as separate observations). f_{GPS} = factor multiplied by formal standard deviation for weighting. χ^2 with data type subscript are χ^2 divided by the number of observations for the data type. χ^2 without a subscript is total χ^2 for the model. N_{data} = a total number of observations. N_{p} = number of free parameters. DOF = degree of freedom (number of observations minus the number of free parameters). $\chi_v{}^2$ is the reduced chi-square (total χ^2 divided by DOF).

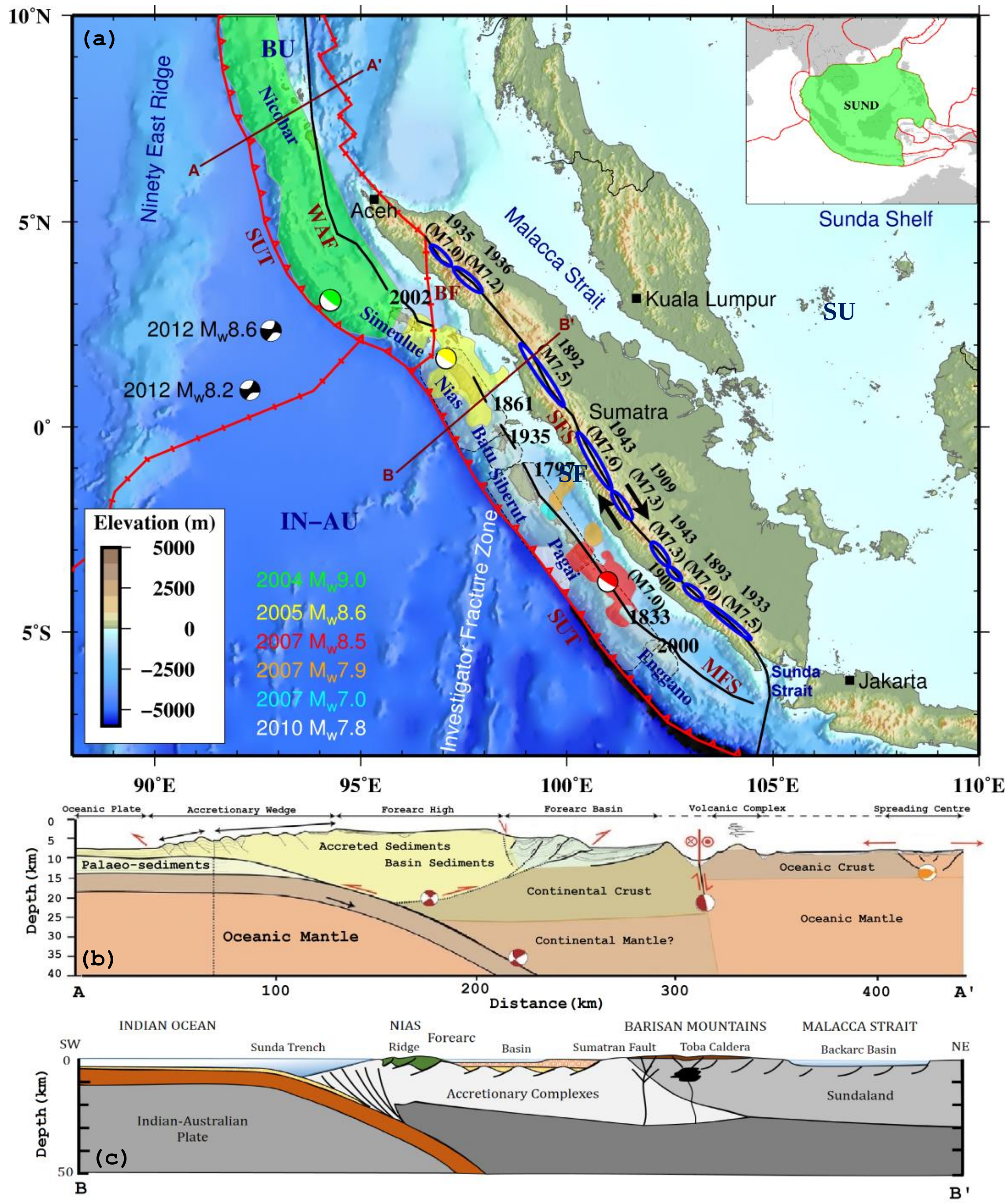

Figure 1. (a) Topographic map of Sumatra and the surrounding archipelago (top). The inset is a regional map where the green polygon indicates the boundary of the Sunda plate. The focal mechanisms are sourced from the gCMT Catalogue [*Ekström et al.*, 2012]. The regions of coloured outlines indicate the rupture zone of large historic and recent ruptures on the Sunda megathrust, modified from *Briggs et al.* [2006], *Hurukawa et al.* [2014] and *Feng et al.* [2015]. Abbreviations: WAF = West Andaman fault; BF = Batee fault; SFS = Sumatra fault system; MFS = Mentawai fault system from *Coffin et al.* [1998] and *McCaffrey* [2009b]. SUT = Sunda trench; IN–AU = Indian–Australian plate; BU = Burma block; SU = Sunda block; SF = Sunda forearc sliver block. 1797 ~M 8.7; 1833 ~M 8.9; 1861 ~M 8.5 1935, ~M_w 7.7 2000, M_w 7.9 and 2002 M_w 7.3. The schematic cross-sections A–A' and B–B' are modified from **(b)** *Singh and Moeremans* [2017, Figure 13.2], and **(c)** *Simandjuntak and Barber* [1996, Figure 9b].

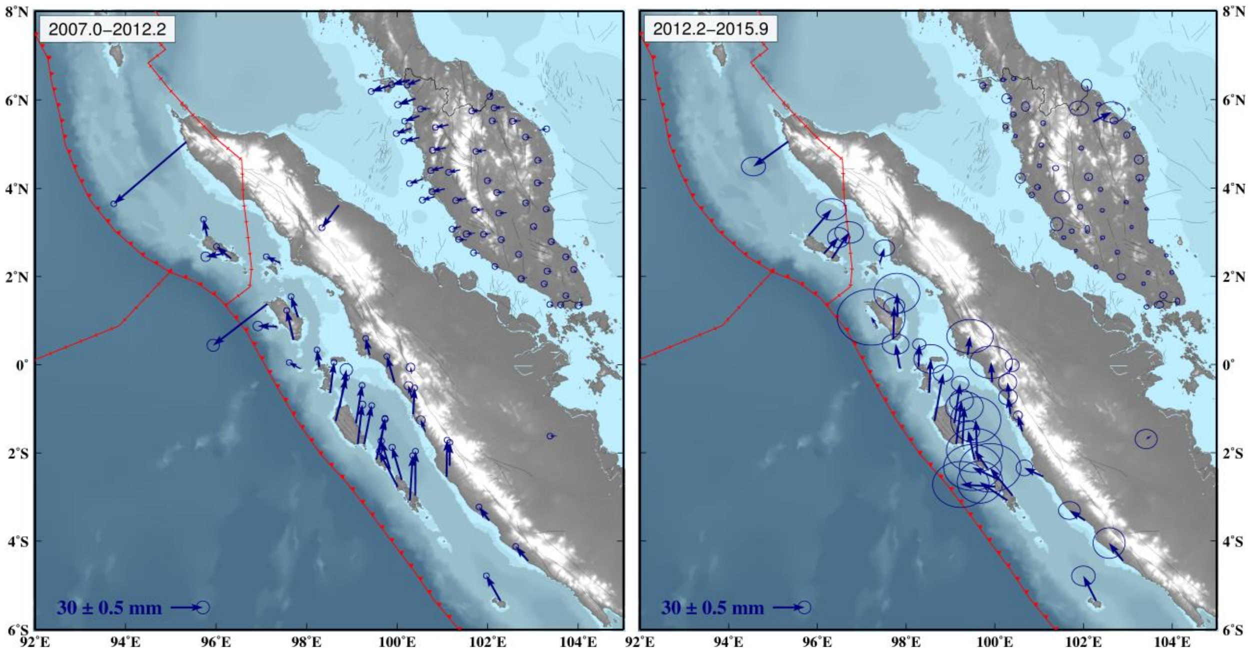

Figure 2. The velocity fields in Peninsular Malaysia, Sumatra and Sunda forearc archipelagos. All velocities are shown relative to the Sunda Plate. Error ellipses illustrate at 68% confidence interval.

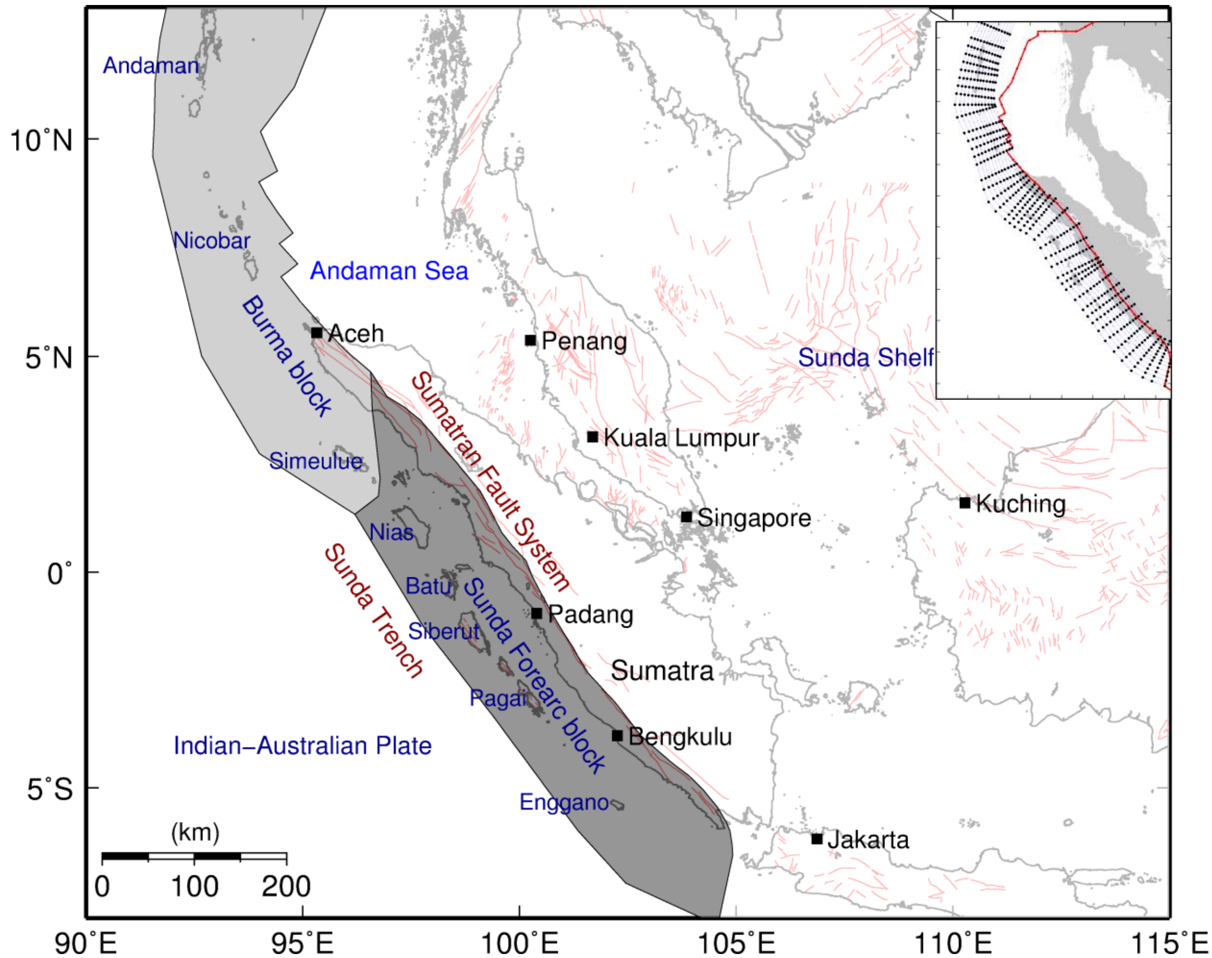

Figure 3. Elastic crustal block configuration described in this study. The surface traces of known fault lines are shown as red lines [*Coffin et al.*, 1998; *JMG*, 2009; *McCaffrey*, 2009b]. The backarc spreading ridge and transform fault in Andaman Sea as in *Bird* [2003, Figure 4]. Inset illustrates the slab geometry of the Sunda subduction trench outlined by nodes (black dots), and the red line is the boundary of the Sunda block.

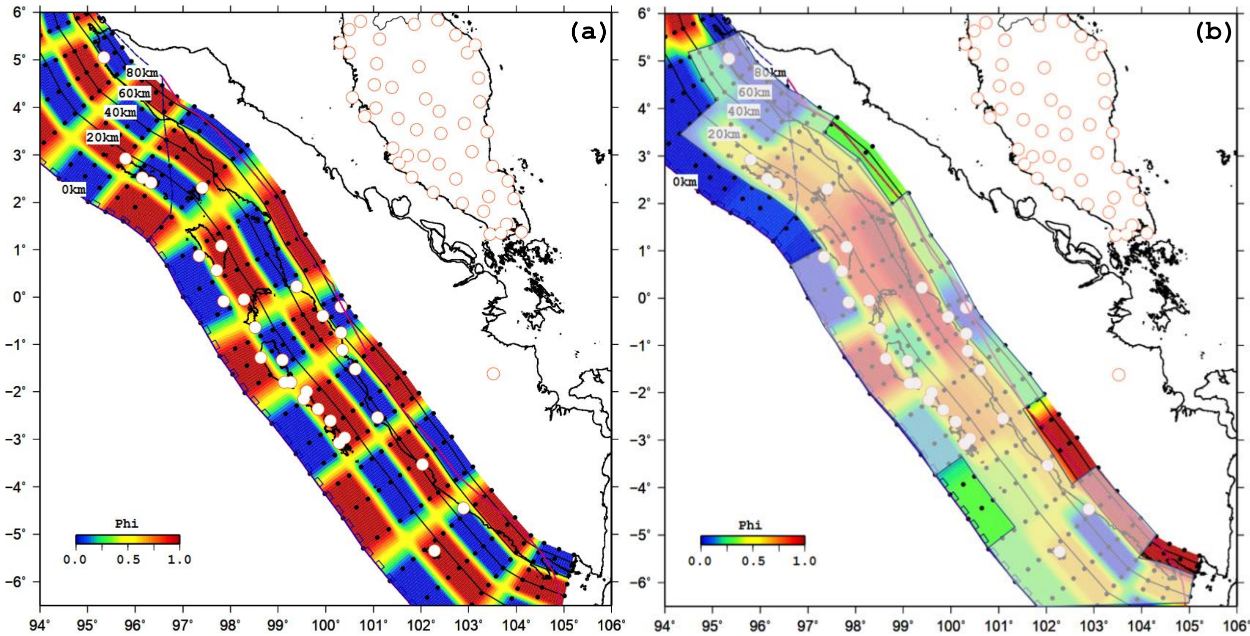

Figure 4. Results of the checkerboard test for locking on the Sunda subduction interface. **(a)** the synthetic input locking pattern designated by Phi (Φ). Each patch covers an area of approximately 150 x 20 km. **(b)** the recovered locking distribution from inversion of the white noise data generated by the forward model. The transparent grey area shows the resolved patches of the slab. Phi (Φ) refers to the degree of coupling, where Φ value of 1.0 means full interseismic coupling, and 0 means no coupling (aseismic creep). The white circles indicate the available sites in this study.

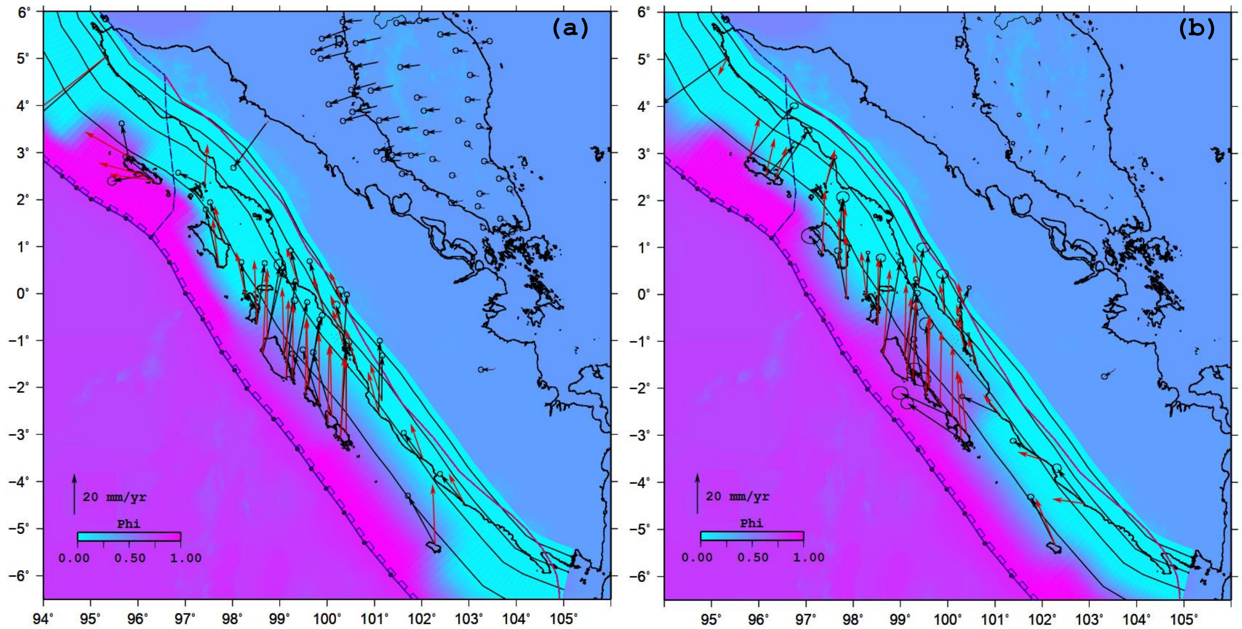

Figure 5. The cGPS site velocities in black arrows (1σ uncertainties) with calculated velocities in red arrows are relative to the Sunda plate in the order of: **(a)** 2007.0–2012.2 and **(b)** 2012.2–2015.9. The shading on the Sunda forearc represents the level of coupling coefficient, phi Φ, where the value indicates freely slipping at 0 and fully locked at 1. The pole of rotation for the Sunda block was based on *Yong et al.* [2017]. The black lines indicate slab contours with 20 km interval start from 0 km at the surface.

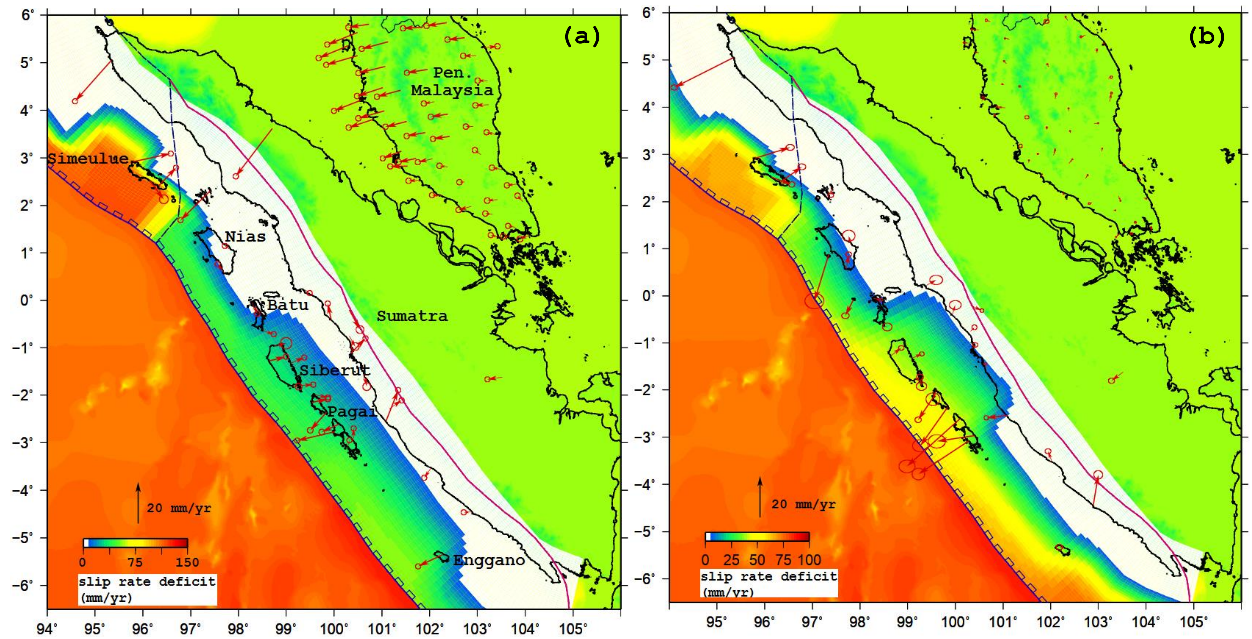

Figure 6. The colour bar indicates the slip rate deficit (in mm/yr) along the Sumatra subduction zone. The cGPS vector residuals (observed-modelled) shown in red arrows with 1σ uncertainties.

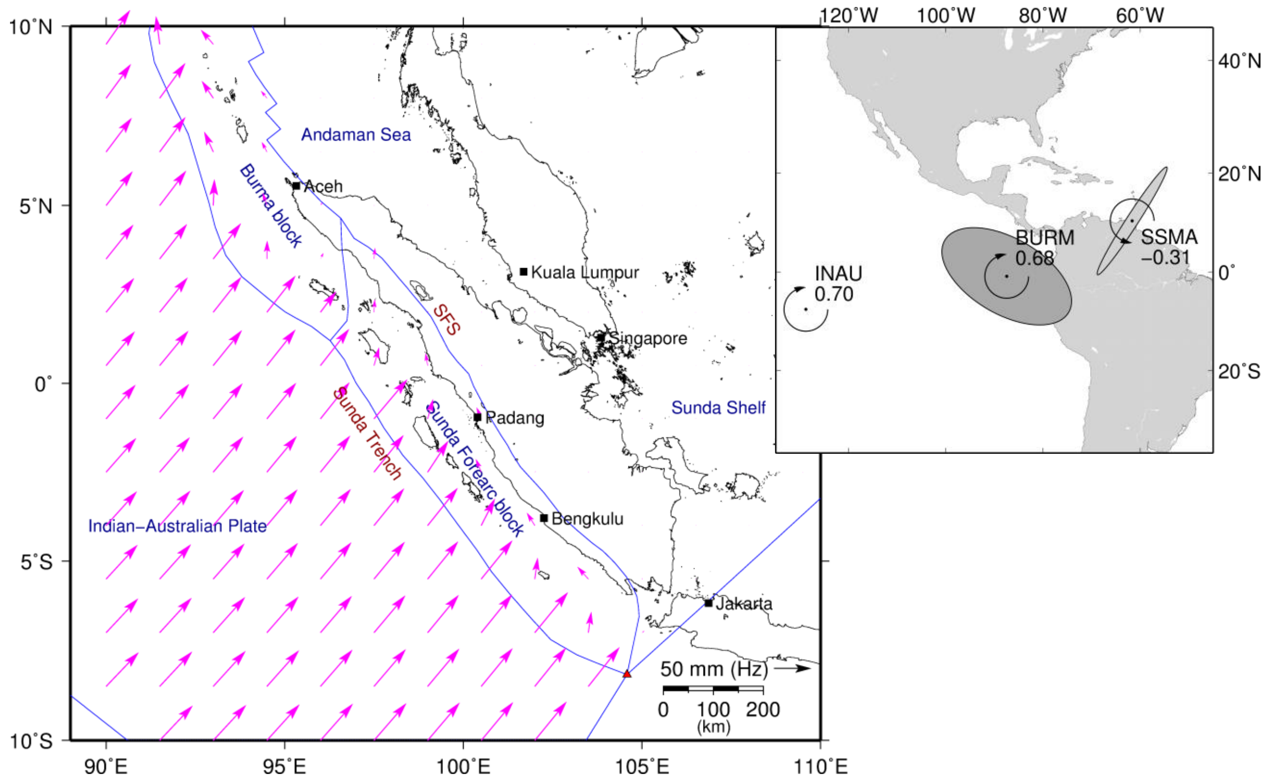

Figure 7. The modelled interseismic velocity field (magenta arrows) after the 2012 Wharton Basin earthquakes, which represents the most recent velocity field relative to the Sunda plate. The inset shows the locations and error ellipses of the poles of rotation for each tectonic block relative to the Sunda plate. Rotation rates (°/Ma) are indicated with the ellipses uncertainties (positive indicates counter-clockwise rotation). Abbreviation: SFS = Sumatran fault system; INAU = Indian–Australian plate; BURM = Burma plate; SSMA = Sunda forearc sliver block.

An Estimate of the Coupling of the Sunda Subduction Zone from Campaign and Continuous GPS Data (1991 – 2016)

C. Z. Yong[1], P. H. Denys[1], and C. F. Pearson[1]

[1]*National School of Surveying, University of Otago, Dunedin, New Zealand*

Supplementary Materials

The supplementary material contains the location map of all the available GPS sites (Figure S1). Figure S2 shows the published vectors (from Prawirodirdjo et al., 2010) for the years 1991–2001 and 2001–2007. Table S1 tabulates the estimated cGPS velocity data relative to Sunda plate fixed. Table S2 gives the nodes of the fault plane of the Sundaland subduction trench for each depth level. Figure S3 shows the level of coupling coefficient along the Sunda subduction interface based on the geodetic-based vectors shown in Figure S2. Figure S4 illustrates the slip rate deficit along the subduction zone.

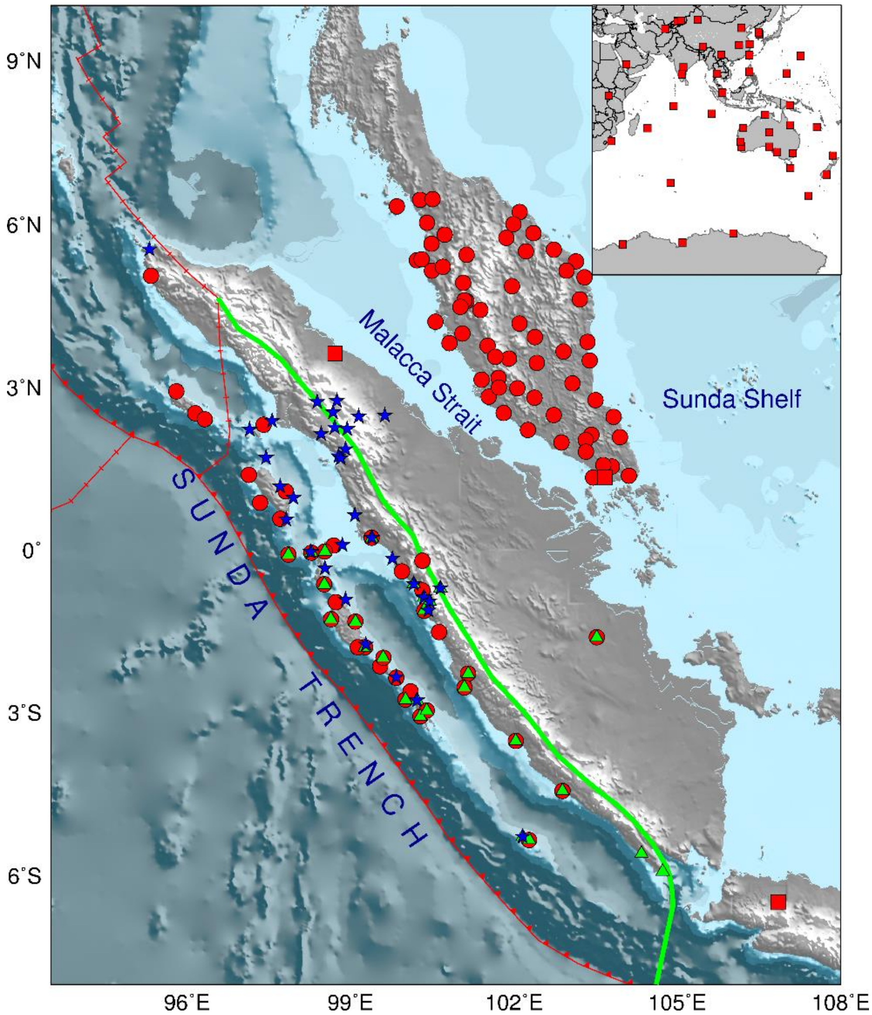

Figure S1: Location map of the cGPS sites used in this study (red circles), IGS station (red squares), and the combined cGPS and campaign-based GPS measurements from Prawirodirdjo et al. (2010) between 1991–2001 (blue stars) and 2001–2007 (green triangles). The selected IGS network (red squares) sites are shown in the inset. The red lines indicate the plate boundaries defined in Bird (2003). The green line represents the Great Sumatran fault from Coffin et al., (1998) and McCaffrey et al., (2009).

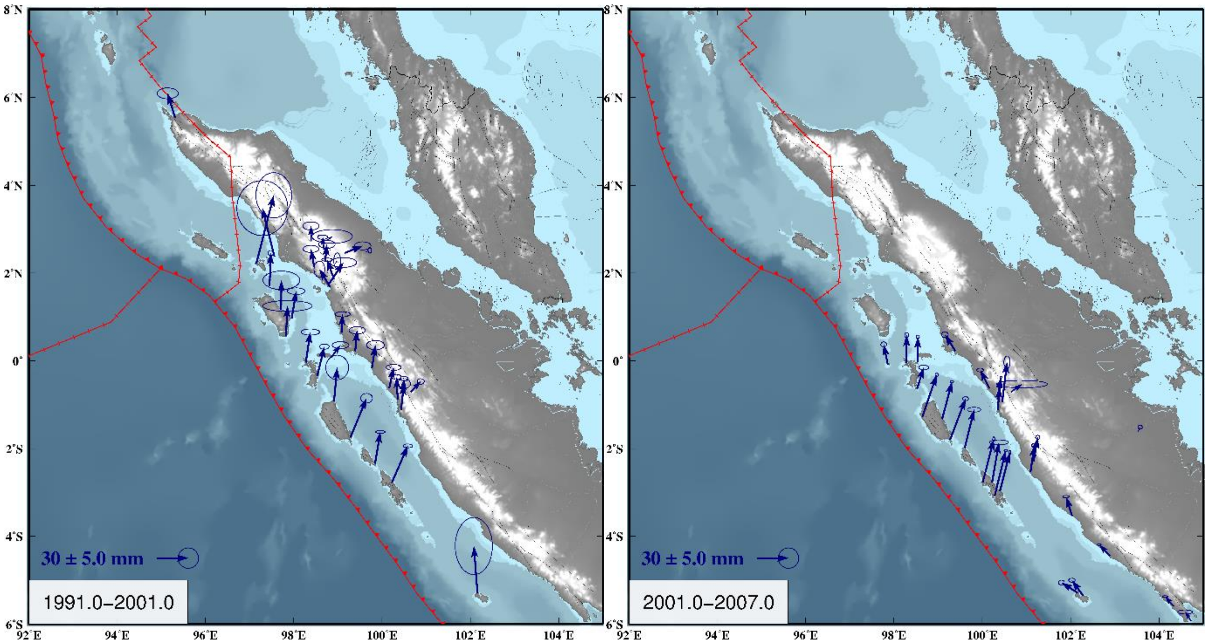

Figure S2: Velocity fields published in Prawirodirdjo et al. (2010). All velocities are shown relative to the Sunda Plate. Error ellipses illustrate at 68% confidence interval.

Table S1: GPS velocities estimated in this study with respect to Sunda plate fixed with 68% confidence interval. The columns are: cGPS site [site], longitude [lon], latitude [lat], velocity [V_E, V_N] (mm/yr), uncertainty [σ_E, σ_N] (mm/yr), and data span (decimal year).

site	lon	lat	V_E	V_N	σ_E	σ_N	V_E	V_N	σ_E	σ_N
			2007.0 – 2012.2				**2012.2 – 2016.0**			
ABGS	99.39	0.22	-3.57	15.86	0.22	0.22	2.14	17.72	1.81	1.31
ARAU	100.28	6.45	-16.99	-4.46	0.23	0.23	-4.02	-0.13	0.19	0.15
AYER	101.86	5.75	-9.02	0.06	0.23	0.23	1.39	2.17	0.74	0.56
BABH	100.49	5.15	-14.27	-3.52	0.22	0.22	-0.98	1.03	0.14	0.12
BAHA	102.38	2.81	-3.45	1.24	0.23	0.23	2.09	2.87	0.16	0.14
BANT	101.54	2.83	-7.75	0.58	0.22	0.22	0.52	2.04	0.16	0.14
BEHR	101.52	3.77	-9.58	-1.90	0.23	0.23	-0.13	1.25	0.58	0.48
BENT	101.91	3.53	-8.40	-0.90	0.23	0.23	0.52	1.76	0.20	0.18
BITI	97.81	1.08	-6.52	19.66	0.22	0.22	-0.68	22.63	1.78	1.55
BNON	96.15	2.52	-16.08	-2.84	0.37	0.37	13.98	15.09	0.86	0.78
BSAT	100.28	-3.08	2.68	42.95	0.22	0.22	-26.09	17.41	1.77	1.64
BSIM	96.33	2.41	-13.58	11.52	0.22	0.22	16.33	24.59	1.12	0.84
BTET	98.64	-1.28	10.03	41.54	0.22	0.22	8.28	45.37	0.79	0.65
BTHL	97.71	0.57	-6.33	27.83	0.22	0.22	0.96	31.85	0.82	0.65
BUKT	100.32	-0.20	-1.02	5.97	0.33	0.33	3.10	7.84	0.54	0.50
CAME	101.39	4.42	-10.69	-2.29	0.23	0.23	-0.78	1.31	0.24	0.20
CARI	92.72	11.61	-15.02	21.65	0.22	0.22	-13.87	19.84	0.42	0.41
CENE	103.24	4.12	-6.01	0.22	0.23	0.23	1.11	4.78	0.30	0.24
GAJA	103.42	2.12	-4.44	0.17	0.24	0.24	1.46	-1.53	0.14	0.15
GETI	102.11	6.23	-2.57	-6.47	0.23	0.23	-1.70	3.97	0.40	0.46
GMUS	101.96	4.86	-9.46	-0.95	0.22	0.22	-0.46	1.76	0.18	0.16
GRIK	101.13	5.44	-12.02	-2.61	0.22	0.22	-1.75	1.11	0.19	0.18
HAV2	92.98	12.04	-23.62	9.84	0.22	0.22	-17.19	13.07	0.87	0.84
HNKO	97.34	0.87	-17.63	0.42	0.37	0.37	-5.45	8.58	2.65	2.18
HUTB	92.53	10.61	-28.45	35.87	0.22	0.22	-21.75	32.82	2.44	2.05
JHJY	103.80	1.54	-3.15	1.24	0.22	0.22	-0.11	1.32	0.28	0.26
JMBI	103.52	-1.62	-6.12	-0.02	0.22	0.22	-4.58	-2.94	0.86	0.75
JRNT	102.38	3.92	-7.63	-0.64	0.23	0.23	0.13	2.02	0.17	0.16
JUML	102.26	2.21	-4.26	0.86	0.22	0.22	0.73	-0.05	0.14	0.16
KLAW	102.06	2.98	-6.50	-0.90	0.22	0.22	1.07	3.57	0.18	0.30
KRAI	102.22	5.50	-5.08	1.16	0.23	0.23	17.32	9.09	1.09	0.80
KROM	103.50	2.76	-4.04	1.36	0.23	0.23	1.29	1.35	0.15	0.13
KTET	99.84	-2.36	-8.09	26.48	0.24	0.24	-12.59	17.47	2.19	1.71

KUAL	103.14	5.32	6.81	1.13	0.23	0.23	-0.43	1.36	0.14	0.13
KUKP	103.45	1.33	-3.40	1.67	0.22	0.22	-1.22	-0.91	0.19	0.17
LAIS	102.03	-3.53	-9.38	12.81	0.22	0.22	-14.74	9.35	0.85	0.69
LASA	101.07	4.92	-12.18	-2.32	0.23	0.23	-0.87	2.09	0.17	0.17
LEWK	95.80	2.92	-3.30	15.96	0.22	0.22	21.79	25.03	1.17	0.83
LGKW	99.85	6.33	-17.96	-5.91	0.22	0.22	-5.00	-0.60	0.24	0.24
LHWA	97.13	1.38	-50.56	-39.44	0.47	0.47	-	-	-	-
LIPI	102.10	4.18	-4.53	-0.19	0.23	0.23	0.54	3.10	0.31	0.29
LNNG	101.16	-2.29	0.15	22.17	0.22	0.22	-	-	-	-
MERS	103.83	2.45	-4.43	-0.06	0.23	0.23	1.53	1.10	0.13	0.12
MERU	101.41	3.14	-8.34	-2.64	0.22	0.22	-0.61	1.85	0.48	0.52
MKMK	101.09	-2.54	0.57	34.93	0.22	0.22	-17.91	8.28	0.65	0.62
MLKN	102.28	-5.35	-13.11	23.90	0.22	0.22	-12.01	23.71	0.92	0.77
MNNA	102.89	-4.45	-11.48	13.91	0.22	0.22	-13.27	17.10	1.25	1.19
MSAI	99.09	-1.33	5.68	36.25	0.22	0.22	5.41	37.79	0.68	0.58
MUAD	103.07	3.07	-2.36	2.72	0.23	0.23	0.58	1.96	0.12	0.13
MUKH	103.21	4.62	-4.28	0.67	0.23	0.23	1.65	1.03	0.36	0.34
NGNG	99.27	-1.80	7.09	36.83	0.22	0.22	1.86	35.42	1.47	1.18
NTUS	103.68	1.35	-2.72	0.54	0.23	0.23	0.88	0.19	0.37	0.26
PARY	100.32	-0.75	-2.95	11.48	0.33	0.33	-1.34	14.46	0.71	0.69
PASP	102.36	5.84	-9.25	-0.90	0.23	0.23	-0.88	2.27	0.18	0.15
PBJO	98.52	-0.64	3.66	29.30	0.22	0.22	1.54	32.29	1.32	1.12
PBLI	97.41	2.31	-12.79	6.00	0.22	0.22	4.23	13.99	0.80	0.63
PDIC	101.81	2.53	-5.16	0.47	0.23	0.23	0.70	2.17	0.11	0.11
PEKN	103.39	3.49	-4.13	1.67	0.22	0.22	1.02	1.67	0.11	0.10
PKRT	99.54	-2.15	8.12	38.40	0.24	0.24	-5.95	27.27	0.89	0.79
PPNJ	99.60	-1.99	5.54	32.67	0.22	0.22	-1.22	30.95	1.95	1.79
PRKB	100.40	-2.97	0.19	42.43	0.22	0.22	-21.50	26.46	2.40	1.89
PRTS	102.87	1.98	-5.51	-1.05	0.23	0.23	-0.86	0.43	0.32	0.23
PSKI	100.35	-1.12	1.58	25.02	0.22	0.22	-2.30	16.15	0.72	0.63
PSMK	97.86	-0.09	-10.32	5.92	0.22	0.22	-4.10	23.22	1.05	0.80
PTLO	98.28	-0.05	-2.13	16.35	0.22	0.22	0.72	21.38	0.52	0.44
PUPK	100.56	4.21	-12.11	-4.15	0.22	0.22	0.76	0.59	0.39	0.39
PUSI	101.02	4.48	-11.70	-3.30	0.23	0.23	-0.54	1.01	0.15	0.14
RNGT	92.91	12.51	-	-	-	-	24.56	-3.29	10.80	14.68
SAMP	98.71	3.62	-15.82	-21.49	0.23	0.23	-	-	-	-
SBKB	100.82	3.81	-11.07	-3.10	0.23	0.23	0.50	1.40	0.21	0.22
SEG1	102.73	2.49	-1.93	0.63	0.23	0.23	1.43	2.46	0.17	0.16
SETI	102.73	5.53	-7.68	-0.41	0.23	0.23	-1.93	-0.32	0.31	0.26
SGPT	100.49	5.64	-13.80	-5.02	0.22	0.22	-3.02	0.89	0.21	0.19
SIK1	100.73	5.81	-9.16	-0.72	0.23	0.23	-1.65	1.39	0.31	0.37
SLBU	100.01	-2.77	-17.26	33.97	0.22	0.22	-32.86	2.16	2.20	1.79
SMGY	100.10	-2.61	-8.97	30.98	0.24	0.24	-25.44	11.64	2.26	1.79
SPGR	103.32	1.81	-3.03	1.07	0.23	0.23	1.31	1.00	0.14	0.14
SRIJ	102.91	3.66	-3.05	0.55	0.23	0.23	2.29	0.74	0.16	0.13
TERI	102.97	5.15	-5.69	0.42	0.23	0.23	0.23	2.11	0.23	0.25
TGPG	104.11	1.37	-4.53	-1.15	0.25	0.25	0.47	2.60	0.17	0.26
TGRH	103.95	2.08	-2.08	3.38	0.23	0.23	1.70	0.41	0.15	0.15
TIKU	99.94	-0.40	-7.09	24.79	0.22	0.22	-1.11	19.05	1.66	1.26
TLKI	101.05	3.99	-11.75	-2.81	0.23	0.23	-3.76	1.26	0.22	0.21
TLLU	99.13	-1.80	4.13	37.67	0.28	0.28	5.06	41.54	0.93	0.84
TLOH	102.42	3.45	-7.50	-0.49	0.22	0.22	0.06	1.87	0.16	0.14
TNTI	98.73	-0.97	6.19	36.01	0.48	0.48	-	-	-	-
TOKA	100.40	6.03	-16.32	-5.77	0.25	0.25	-5.72	-0.33	0.36	0.37
TRTK	100.62	-1.52	-4.11	11.12	0.33	0.33	-4.21	15.37	0.35	0.35
UMLH	95.34	5.05	-67.72	-59.02	0.22	0.22	-33.06	-23.68	0.94	0.73
UPMS	101.72	2.99	-8.03	-0.98	0.25	0.25	0.60	1.40	0.19	0.17
USMP	100.30	5.36	-13.49	-5.00	0.23	0.23	-2.61	0.94	0.19	0.17
UUMK	100.51	6.46	-12.26	-5.32	0.22	0.22	-3.57	0.49	0.17	0.15

Table S2: The table of nodes (longitude and latitude, decimal degree) represents the fault plane of the Sundaland subduction trench for each depth (km).

Fault: SUMA 1 # of nodes: 46 (strike); 12 (dip); *overriding*: SSMA; *submerging*: AUST; 0					
Depth: 4 km	Depth: 7 km	Depth: 10 km	Depth: 14 km	Depth: 19 km	Depth: 25 km
104.580 -8.170	104.662 -7.840	104.729 -7.544	104.790 -7.259	104.865 -6.966	104.908 -6.741
103.760 -7.860	103.901 -7.544	104.023 -7.273	104.137 -7.012	104.262 -6.730	104.351 -6.538
103.180 -7.620	103.344 -7.326	103.491 -7.062	103.641 -6.812	103.794 -6.548	103.908 -6.352
102.450 -7.200	102.673 -6.945	102.873 -6.705	103.070 -6.481	103.270 -6.241	103.416 -6.067
101.860 -6.560	102.127 -6.327	102.349 -6.124	102.570 -5.917	102.802 -5.713	102.966 -5.563
101.350 -5.980	101.621 -5.725	101.841 -5.529	102.067 -5.329	102.293 -5.130	102.465 -4.981
100.790 -5.300	101.085 -5.068	101.324 -4.896	101.563 -4.718	101.806 -4.540	101.999 -4.397
100.360 -4.660	100.646 -4.432	100.884 -4.261	101.122 -4.076	101.360 -3.909	101.555 -3.761
99.980 -4.150	100.261 -3.933	100.493 -3.766	100.743 -3.585	100.969 -3.412	101.171 -3.258
99.670 -3.730	99.960 -3.501	100.193 -3.335	100.443 -3.147	100.667 -2.983	100.879 -2.830
99.370 -3.310	99.655 -3.073	99.888 -2.905	100.141 -2.723	100.362 -2.556	100.573 -2.399
98.870 -2.670	99.160 -2.463	99.388 -2.292	99.645 -2.113	99.859 -1.945	100.070 -1.788
98.300 -2.020	98.592 -1.813	98.835 -1.647	99.086 -1.472	99.308 -1.317	99.529 -1.164
98.040 -1.630	98.344 -1.444	98.595 -1.301	98.866 -1.143	99.102 -1.008	99.330 -0.873
97.770 -1.250	98.100 -1.084	98.362 -0.960	98.636 -0.820	98.888 -0.694	99.121 -0.570
97.370 -0.550	97.727 -0.370	97.990 -0.236	98.258 -0.109	98.513 0.022	98.735 0.137
97.000 0.001	97.345 0.175	97.620 0.314	97.881 0.447	98.134 0.576	98.360 0.691
96.667 0.666	96.996 0.868	97.258 1.030	97.506 1.186	97.746 1.337	97.961 1.473
96.270 1.200	96.545 1.471	96.765 1.687	96.976 1.891	97.180 2.088	97.364 2.263
95.750 1.600	95.998 1.896	96.196 2.132	96.385 2.356	96.568 2.574	96.731 2.768
95.380 1.800	95.628 2.096	95.826 2.332	96.015 2.556	96.198 2.774	96.361 2.968
95.010 2.010	95.258 2.306	95.457 2.542	95.645 2.766	95.828 2.984	95.991 3.178
94.700 2.250	94.948 2.546	95.147 2.782	95.335 3.006	95.518 3.224	95.681 3.418
94.400 2.500	94.648 2.796	94.847 3.032	95.035 3.256	95.218 3.474	95.382 3.668
93.800 3.000	94.083 3.263	94.308 3.473	94.523 3.673	94.731 3.867	94.917 4.040
93.350 3.600	93.667 3.821	93.920 3.998	94.160 4.166	94.394 4.329	94.602 4.475
93.050 4.400	93.362 4.545	93.616 4.663	93.865 4.779	94.109 4.892	94.332 4.996
92.900 5.000	93.155 5.118	93.370 5.218	93.589 5.320	93.810 5.423	94.009 5.515
92.600 6.000	92.855 6.118	93.071 6.218	93.291 6.320	93.512 6.423	93.711 6.515
92.450 6.500	92.708 6.614	92.925 6.710	93.147 6.808	93.370 6.907	93.571 6.996
92.300 7.000	92.588 7.116	92.828 7.212	93.067 7.308	93.306 7.403	93.516 7.487
92.050 7.500	92.344 7.600	92.589 7.684	92.833 7.767	93.077 7.850	93.291 7.924
91.800 8.000	92.096 8.095	92.343 8.175	92.589 8.254	92.834 8.333	93.050 8.402
91.350 9.000	91.650 9.085	91.900 9.156	92.149 9.226	92.398 9.297	92.617 9.359
91.200 9.800	91.513 9.800	91.773 9.800	92.033 9.800	92.292 9.800	92.520 9.800
91.300 10.500	91.583 10.464	91.822 10.434	92.064 10.404	92.309 10.373	92.527 10.345
91.400 11.000	91.659 10.967	91.881 10.939	92.111 10.911	92.345 10.881	92.555 10.855
91.500 11.500	91.760 11.466	91.982 11.437	92.212 11.407	92.445 11.376	92.656 11.349
91.600 12.000	91.859 11.960	92.081 11.925	92.310 11.890	92.544 11.854	92.754 11.821
91.750 12.500	91.985 12.443	92.189 12.393	92.403 12.341	92.622 12.288	92.822 12.239
91.900 13.000	92.115 12.935	92.304 12.878	92.504 12.818	92.711 12.755	92.901 12.698
92.050 13.500	92.264 13.429	92.451 13.367	92.649 13.300	92.854 13.231	93.043 13.168
92.250 14.000	92.465 13.932	92.653 13.873	92.853 13.810	93.061 13.744	93.251 13.684
92.700 15.000	92.910 14.916	93.094 14.844	93.289 14.766	93.492 14.686	93.678 14.612
93.100 16.000	93.323 15.954	93.518 15.913	93.726 15.869	93.941 15.824	94.138 15.782
93.150 17.000	93.380 16.989	93.580 16.979	93.793 16.968	94.014 16.956	94.217 16.944

Depth: 32 km	Depth: 40 km	Depth: 51 km	Depth: 63 km	Depth: 76 km	Depth: 90 km
104.965 -6.516	105.015 -6.299	105.068 -6.052	105.108 -5.870	105.161 -5.663	105.211 -5.435
104.451 -6.320	104.540 -6.116	104.644 -5.895	104.719 -5.717	104.808 -5.517	104.901 -5.317
104.030 -6.145	104.137 -5.956	104.262 -5.749	104.362 -5.574	104.469 -5.385	104.583 -5.189
103.576 -5.884	103.723 -5.710	103.876 -5.535	104.008 -5.374	104.162 -5.192	104.305 -5.028
103.141 -5.403	103.312 -5.253	103.487 -5.092	103.637 -4.957	103.808 -4.796	103.973 -4.653
102.644 -4.815	102.816 -4.669	102.986 -4.515	103.143 -4.375	103.319 -4.217	103.482 -4.074
102.185 -4.254	102.363 -4.125	102.559 -3.979	102.731 -3.858	102.913 -3.719	103.091 -3.583
101.745 -3.619	101.926 -3.485	102.121 -3.343	102.293 -3.219	102.478 -3.071	102.645 -2.952
101.358 -3.118	101.543 -2.990	101.742 -2.844	101.911 -2.719	102.105 -2.576	102.265 -2.457
101.067 -2.697	101.238 -2.562	101.445 -2.412	101.612 -2.290	101.804 -2.145	101.959 -2.031
100.755 -2.263	100.933 -2.142	101.141 -1.988	101.308 -1.860	101.501 -1.713	101.654 -1.603
100.255 -1.656	100.427 -1.524	100.634 -1.374	100.805 -1.246	100.987 -1.099	101.137 -0.999
99.716 -1.033	99.893 -0.908	100.105 -0.766	100.279 -0.643	100.477 -0.509	100.627 -0.409
99.524 -0.762	99.718 -0.646	99.934 -0.521	100.124 -0.416	100.331 -0.296	100.486 -0.208
99.323 -0.473	99.523 -0.370	99.754 -0.261	99.954 -0.154	100.168 -0.051	100.332 0.037
98.945 0.244	99.147 0.345	99.373 0.459	99.584 0.564	99.790 0.669	99.950 0.749
98.569 0.799	98.766 0.900	98.995 1.018	99.210 1.130	99.405 1.231	99.577 1.320
98.159 1.600	98.346 1.719	98.563 1.858	98.766 1.990	98.951 2.109	99.114 2.214
97.534 2.426	97.694 2.578	97.881 2.756	98.058 2.922	98.218 3.073	98.359 3.206
96.882 2.948	97.025 3.118	97.190 3.315	97.347 3.501	97.488 3.669	97.613 3.818
96.512 3.148	96.655 3.318	96.821 3.515	96.977 3.701	97.118 3.869	97.243 4.018
96.142 3.358	96.285 3.528	96.451 3.725	96.607 3.911	96.749 4.079	96.874 4.228
95.833 3.598	95.975 3.768	96.141 3.965	96.297 4.151	96.439 4.319	96.564 4.468
95.533 3.848	95.676 4.018	95.842 4.215	95.998 4.401	96.140 4.569	96.265 4.718
95.090 4.200	95.252 4.351	95.441 4.527	95.619 4.692	95.780 4.842	95.922 4.974
94.795 4.609	94.977 4.736	95.189 4.884	95.388 5.023	95.569 5.149	95.729 5.261
94.532 5.089	94.728 5.180	94.951 5.283	95.161 5.381	95.353 5.470	95.523 5.549
94.201 5.604	94.384 5.689	94.594 5.787	94.794 5.879	94.977 5.964	95.140 6.040
93.903 6.604	94.087 6.689	94.297 6.787	94.497 6.879	94.681 6.964	94.844 7.040
93.765 7.081	93.950 7.163	94.163 7.257	94.364 7.346	94.550 7.428	94.714 7.501
93.700 7.561	93.876 7.632	94.085 7.715	94.284 7.795	94.467 7.868	94.630 7.933
93.479 7.988	93.659 8.049	93.872 8.122	94.076 8.191	94.262 8.255	94.428 8.311
93.239 8.463	93.421 8.521	93.635 8.590	93.840 8.656	94.028 8.716	94.195 8.770
92.809 9.413	92.992 9.465	93.210 9.526	93.417 9.585	93.608 9.639	93.777 9.687
92.720 9.800	92.911 9.800	93.138 9.800	93.354 9.800	93.552 9.800	93.729 9.800
92.720 10.321	92.906 10.298	93.123 10.270	93.330 10.244	93.521 10.220	93.691 10.199
92.742 10.831	92.926 10.808	93.135 10.782	93.336 10.757	93.521 10.733	93.687 10.712
92.843 11.324	93.027 11.300	93.237 11.273	93.438 11.247	93.623 11.222	93.789 11.201
92.941 11.792	93.124 11.764	93.334 11.731	93.534 11.700	93.719 11.672	93.885 11.646
92.999 12.196	93.175 12.153	93.377 12.104	93.570 12.057	93.748 12.013	93.908 11.974
93.072 12.646	93.243 12.595	93.437 12.536	93.623 12.480	93.796 12.427	93.951 12.381
93.212 13.111	93.381 13.054	93.574 12.988	93.758 12.926	93.930 12.867	94.083 12.815
93.421 13.630	93.592 13.577	93.786 13.515	93.973 13.456	94.146 13.402	94.300 13.353
93.844 14.546	94.011 14.480	94.201 14.405	94.383 14.333	94.552 14.266	94.703 14.206
94.314 15.744	94.491 15.706	94.692 15.662	94.886 15.620	95.065 15.581	95.225 15.546
94.398 16.932	94.580 16.920	94.787 16.907	94.986 16.893	95.170 16.879	95.335 16.867

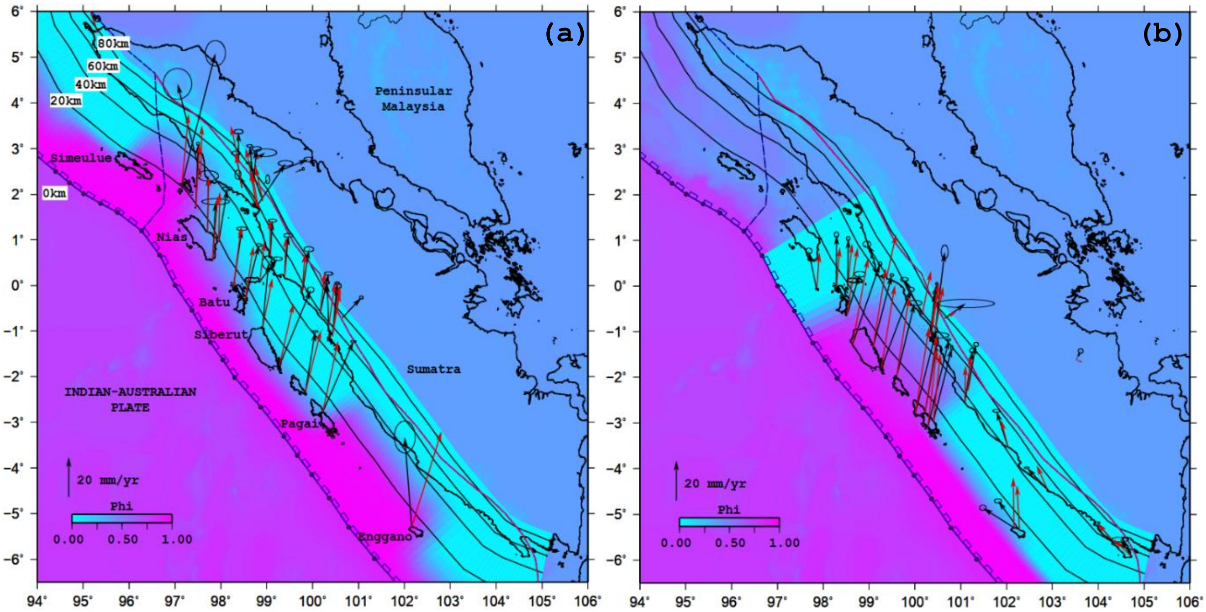

Figure S3: The cGPS site velocities (black arrows; 1σ uncertainties) with calculated velocities (red arrows) are relative to the Sunda plate in the order of: **(a)** 1991.0 – 2001.0 and **(b)** 2001.0 – 2007.0. The shading on the Sunda forearc represents the level of coupling coefficient Φ, where the value indicates freely slipping at 0 and fully locked at 1.

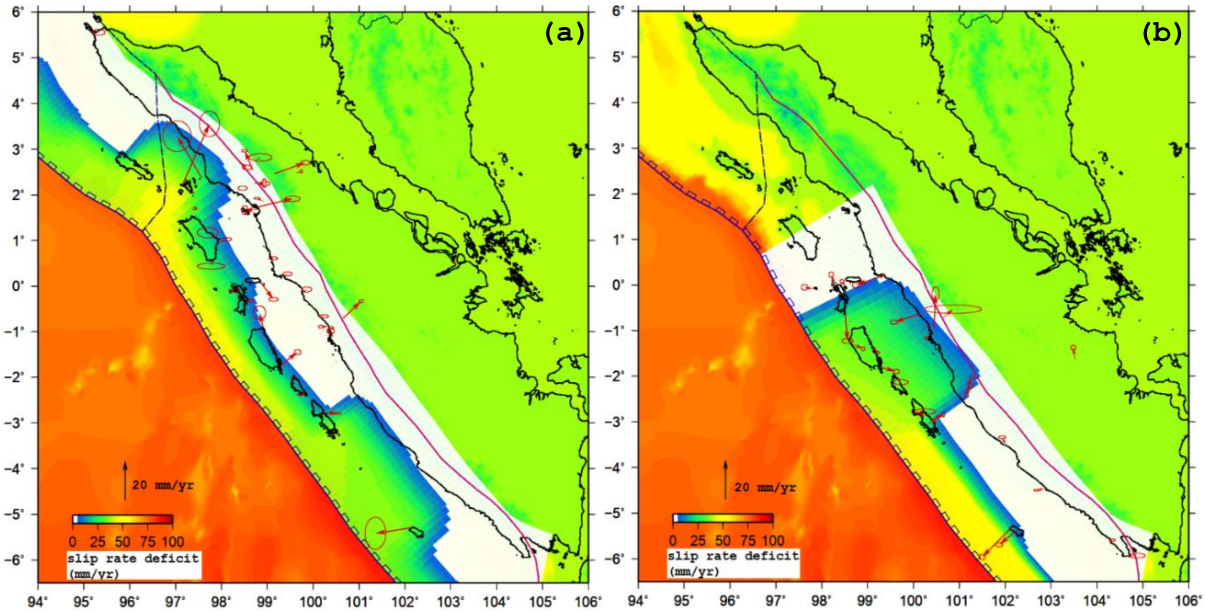

Figure S4: The colour bar indicates the slip rate deficit (mm/yr) along the Sumatra subduction zone in the order of: **(a)** 1991.0 – 2001.0 and **(b)** 2001.0 – 2007.0. The cGPS vector residuals (observed-modelled) shown in red arrows (1σ uncertainties).